Mass conservative BDF-discontinuous Galerkin/explicit finite volume schemes for coupling subsurface and overland flows

P. Sochala, A. Ern, S. Piperno. *

Université Paris-Est, CERMICS, Ecole des Ponts, Champs sur Marne, 77455 Marne la Vallée Cedex 2, France

Abstract

Robust and accurate schemes are designed to simulate the coupling between subsurface and overland flows. The coupling conditions at the interface enforce the continuity of both the normal flux and the pressure. Richards' equation governing the subsurface flow is discretized using a Backward Differentiation Formula and a symmetric interior penalty Discontinuous Galerkin method. The kinematic wave equation governing the overland flow is discretized using a Godunov scheme. Both schemes individually are mass conservative and can be used within single-step or multi-step coupling algorithms that ensure overall mass conservation owing to a specific design of the interface fluxes in the multi-step case. Numerical results are presented to illustrate the performances of the proposed algorithms.

Key words: surface-subsurface coupled flows, Richards' equation, variably saturated porous medium, kinematic wave equation, Discontinuous Galerkin method, unstructured mesh
PACS: 92.40.Kf, 92.40.Qk, 47.56.+r

1 Introduction

The interactions of subsurface and overland flows are an important ingredient for a comprehensive understanding of hydrology processes. While there is an extensive bulk of literature devoted to the numerical study of water flows in single-phase and variably saturated porous media, the issue of coupling such flows with surface flows generated by rivers, tides or floods has received less

* corresponding author: serge.piperno@enpc.fr

attention. One of the most popular ways to couple Darcy and Stokes flows is through the well-known Beavers–Joseph–Saffman condition [8,29,19]. This condition was used for instance in [13,25] in the mathematical and numerical study of the coupling of Darcy flow with a three-dimensional non-hydrostatic shallow-water model. Another approach used in numerical hydrology (see among others [31]) considers discontinuous pressures at the interface and evaluates an interface flux as the pressure difference, multiplied by an exchange coefficient depending on the soil relative permeability. A third approach consists in assuming both normal flux and pressure continuity. This means that the hydraulic head of the subsurface flow matches the depth of the overland flow at the interface, while the normal ground flow velocity at the interface is used as a source term in the governing equation of the overland flow. Examples of studies based on this approach include coupling one-dimensional surface flow with vertical soil columns [30], coupling the two-dimensional Richards' equation with a one-dimensional kinematic or diffusive wave approximation for the overland flow [23,7], and coupling the two-dimensional Darcy's equation with one-dimensional shallow-water equations [11].

In the present work, we assume that the subsurface flow occurs in a variably saturated porous medium and that this flow can be described by Richards' equation, entailing in particular that there are no trapped air pockets in the soil; otherwise more general multi-phase models should be used [3]. Furthermore the kinematic wave approximation is used to describe the overland flow. This choice is solely made for ease of exposition and more general shallow water models can also be used. Concerning the coupling conditions, we adopt the third approach described above, namely enforcing the continuity of both normal flux and pressure at the interface. These coupling conditions are generally valid when the overland flow is mainly produced by exfiltration from the soil, so that normal flux and pressure equilibrium can be expected to hold at all times. A different situation, which falls beyond the present scope, is that of a runon surface wave rapidly propagating over a dry soil.

Many methods can be employed to discretize in space Richards' equation, namely finite differences [32,9], finite volumes (FV) [24], finite elements (FE) [9,20] or mixed finite elements (MFE) [22,6]. These methods are generally combined with an implicit Euler time scheme. An alternative approach for space discretization is to use a discontinuous Galerkin (DG) method. Advantages offered by DG methods include local (elementwise) conservation (as FV and MFE), high-order accuracy (as FE and MFE), and flexibility in the use of non-matching meshes (as FV), in particular within multi-physics and multi-domain approaches. Various forms of DG methods can be used for Richards' equation and more generally for two-phase flows in porous media. Examples include the so-called Local Discontinuous Galerkin method [16,4] and the non-symmetric or the symmetric interior penalty DG method [21,2,5]. In the present work, we choose the symmetric interior penalty DG method (in short SIPG), because it

preserves the natural symmetry in the discrete diffusion operator. Regarding time discretization, the common approach when working with DG methods is to employ Runge-Kutta (RK) explicit schemes [10] or diagonally implicit ones [2]. Here, we propose instead to use a backward differentiation formula (BDF). We think that this approach offers several advantages, such as high-order accuracy in the time discretization, circumventing the CFL condition which can be very restrictive for explicit schemes when diffusion processes are dominant, and in general higher computational efficiency than implicit RK schemes for problems where the nonlinear solver is expensive. Typically, if piecewise polynomials of degree p are used in the DG method, a BDF of order $(p+1)$ can be employed.

The main objective of this work is to design robust and accurate schemes for coupling subsurface and overland flows. While Richards' equation is discretized by a BDF-SIPG method, the overland flow governing equation is discretized by a Godunov scheme and advanced in time with a different time step if the overland flow time scale is quite different from the subsurface flow time scale. Two important issues are addressed in the design of our coupling algorithms: 1) to satisfy as accurately as possible the coupling conditions which impose certain specific inequality and equality constraints on the pressures and normal fluxes, similarly to the boundary conditions encountered in Signorini problems, and 2) to ensure overall mass conservation for the whole system consisting of subsurface and overland flows. This point deserves some particular attention. Indeed, although mass conservative schemes are used for both subsurface and overland flows, the interface flux must be chosen appropriately when working with multi-step methods such as BDFs. For simplicity, we discuss in detail only the design of the interface flux for the second-order BDF. Furthermore, only constant time steps are considered, but the present algorithms can be readily extended to accommodate variable time steps. Finally, although the material is presented in a 2D/1D setting (that is, a two-dimensional subsurface flow coupled to a one-dimensional overland flow), the results extend naturally to the 3D/2D setting. In particular, the wet part of the interface is not tracked directly, but is determined at each time step by a cell-oriented procedure within an iterative loop that solves consecutively the overland and subsurface flow governing equations.

This paper is organized as follows. In Section 2, we present the physical problem. In Section 3, we describe the time and space discretization of the model problem and design the coupling algorithms for both first-order and second-order BDFs. Finally, in Section 4, we present numerical results assessing the performance of the proposed algorithms on three test cases.

2 Model problem

2.1 The setting

Let $\Omega \subset \mathbb{R}^2$ denote the bounded subsurface flow domain with outward normal unit vector n_Ω. The boundary of Ω is divided into three parts (see Figure 1): $\mathcal{I}$ is the upper part of the boundary where overland flow can occur, $\mathcal{W}$ are lateral walls, and $\mathcal{B}$ represents the lower part of the boundary. At any time t, the set $\mathcal{I}$ is divided into "wet" and "dry" parts $\mathcal{I}^{\mathrm{d},t} \cup \mathcal{I}^{\mathrm{w},t}$, with

$$\mathcal{I}^{\mathrm{w},t} \stackrel{\mathrm{def}}{=} \{x \in \mathcal{I};\ h(x,t) > 0\} \quad \text{and} \quad \mathcal{I}^{\mathrm{d},t} \stackrel{\mathrm{def}}{=} \{x \in \mathcal{I};\ h(x,t) = 0\}, \tag{1}$$

where h is the depth of the overland flow. Observe that the above partition of $\mathcal{I}$ is time-dependent.

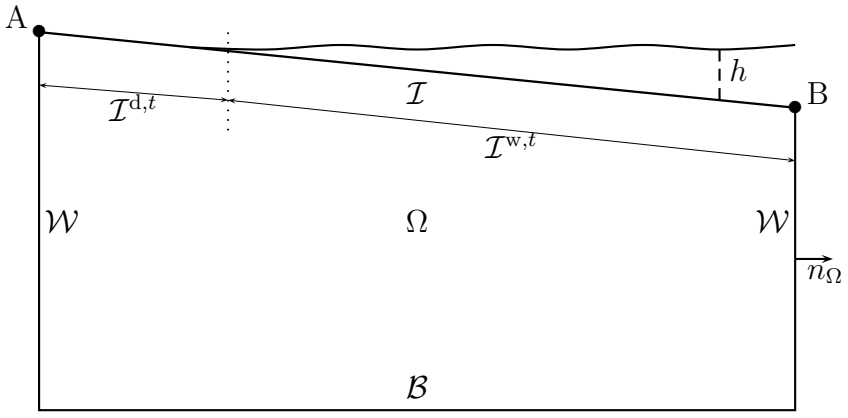

Figure 1. Schematic of the computational domain with basic notation.

2.2 Subsurface flow

The soil is modeled as a non-deformable porous medium in which the pores can contain both water and air (unsaturated zone) or only water (saturated zone). We assume that water is incompressible and that air pressure does not affect the flow. The water conservation equation takes the form

$$\partial_t[\theta(\psi)] + \nabla \cdot v(\psi) = f, \tag{2}$$

where ∂_t denotes partial time-derivative, ψ is the hydraulic head (m), $\theta(\psi)$ the volumetric water content (dimensionless), $v(\psi)$ the flow velocity (ms^{-1}), and f a volumetric water source or sink (s^{-1}). In the sequel, we assume that there are no volumetric sources or sinks, so that $f = 0$. The flow velocity depends

on the hydraulic head through the generalized Darcy law

$$v(\psi) = -K(\psi)\nabla(\psi + z), \tag{3}$$

where $K(\psi)$ is the (possibly tensor-valued) hydraulic conductivity (ms^{-1}) and z the vertical coordinate (m). Substituting (3) into (2), Richards' equation is obtained in the form [28]

$$\partial_t[\theta(\psi)] - \nabla \cdot (K(\psi)\nabla(\psi + z)) = 0. \tag{4}$$

This is a nonlinear parabolic equation which degenerates into a diffusion equation in the saturated zone where θ and K are constant. Given at each time $t \in [0, T]$, where T is the total simulation time, the partition $\{\mathcal{I}^{\mathrm{w},t}, \mathcal{I}^{\mathrm{d},t}\}$ of $\mathcal{I}$, a Dirichlet datum ω_ψ defined on $\mathcal{I}^{\mathrm{w},t}$ and a Neumann datum ω_v defined on $\mathcal{I}^{\mathrm{d},t}$, the subsurface flow is governed by

$$\begin{cases} \partial_t[\theta(\psi)] + \nabla \cdot v(\psi) = 0 & \text{in } \Omega \times [0, T], \\ v(\psi) = -K(\psi)\nabla(\psi + z) & \text{in } \Omega \times [0, T], \\ \psi(\cdot, 0) = \psi^0 & \text{in } \Omega, \\ v(\psi) \cdot n_\Omega = v_N & \text{on } (\mathcal{W} \cup \mathcal{B}) \times [0, T], \\ v(\psi) \cdot n_\Omega = \omega_v & \text{on } \{(x, t), x \in \mathcal{I}^{\mathrm{d},t}\}, \\ \psi = \omega_\psi & \text{on } \{(x, t), x \in \mathcal{I}^{\mathrm{w},t}\}, \end{cases} \tag{5}$$

where v_N is the possibly time-dependent normal flow velocity prescribed on $\mathcal{W} \cup \mathcal{B}$ and ψ^0 the initial datum. Examples for the two constitutive laws $\psi \mapsto \theta(\psi)$ and $\psi \mapsto K(\psi)$, which are necessary to close the subsurface flow model, are specified in §4.

2.3 Overland flow

Water surface flows are often modeled by a simplified form of the free boundary Navier–Stokes equations. Assuming hydrostatic pressure, negligible vertical velocity gradients, and mild variations of the free surface leads to the well-known shallow-water equations; see, e.g. [17] for a derivation of these equations. Neglecting turbulence effects, the equations expressing the conservation of mass and momentum reduce to

$$\partial_t h + \partial_x q = (v(\psi) - v_{\mathrm{r}}) \cdot n_\Omega, \tag{6}$$

$$\partial_t q + \partial_x \left[\frac{q^2}{h} + \frac{gh^2}{2} \right] = gh(S - J), \tag{7}$$

where q is the discharge ($m^2 s^{-1}$), $v(\psi) \cdot n_\Omega$ the source or sink term (ms^{-1}) resulting from mass transfer between subsurface and overland flows, v_r the possibly time-dependent prescribed rainfall intensity (ms^{-1}), g the gravity acceleration (ms^{-2}), S the possibly space-dependent bottom slope (dimensionless), and finally J (dimensionless) results from friction effects. Note that the mass transfer term $v(\psi) \cdot n_\Omega$ in the mass conservation equation (6) involves the subsurface flow velocity resulting from (5). Infiltration occurs if $v(\psi) \cdot n_\Omega < 0$, whereas exfiltration occurs if $v(\psi) \cdot n_\Omega > 0$. The Manning-Strickler uniform flow formula is chosen to link J and q, and assuming the flux to be uni-directional from left to right so that $q \geq 0$, this yields

$$q = \mathcal{K} h^{5/3} J^{1/2}, \tag{8}$$

where $\mathcal{K}$ is the Strickler coefficient of roughness ($m^{1/3} s^{-1}$).

A common assumption is to neglect inertia and potential energy effects in (7), so that the momentum balance is governed by the equilibrium between slope and friction, that is

$$S = J. \tag{9}$$

Substituting (9) into (8) yields

$$q = \varphi(h, S) \overset{\text{def}}{=} \mathcal{K} h^{5/3} S^{1/2}. \tag{10}$$

Finally, using (10) in (6) leads to the so-called kinematic wave approximation [26]

$$\partial_t h + \partial_x \varphi(h, S) = (v(\psi) - v_\mathrm{r}) \cdot n_\Omega. \tag{11}$$

This scalar conservation law is strictly hyperbolic whenever $h > 0$. In the present case, waves travel rightwards, and a suitable boundary condition consists in prescribing at the point A (see Figure 1) the value of the surface water depth equal to a datum h_A. Let h^0 be the datum for the initial condition. Then, the overland flow is governed by

$$\begin{cases} \partial_t h + \partial_x \varphi(h, S) = (v(\psi) - v_\mathrm{r}) \cdot n_\Omega & \text{on } \mathcal{I} \times [0, T], \\ h(\cdot, 0) = h^0 & \text{on } \mathcal{I}, \\ h(\mathrm{A}, \cdot) = \mathrm{h_A} & \text{at A} \times [0, \mathrm{T}]. \end{cases} \tag{12}$$

2.4 Coupled problem

We refer to the quadruplet $\{\mathcal{I}^{\mathrm{w},t}, \mathcal{I}^{\mathrm{d},t}, \omega_\psi, \omega_v\}$ as the coupling variables. The model problem considered hereafter for coupling subsurface and overland flows

consists in finding functions (ψ, h) and the above coupling variables such that

$$\begin{cases} \psi \text{ solves (5)} & \text{in } \Omega \times [0,T] \text{ with } \omega_\psi = h \text{ and } \omega_v = v_{\mathrm{r}} \cdot n_\Omega, \\ h \text{ solves (12)} & \text{on } \mathcal{I} \times [0,T], \\ (\psi, h) \in \mathcal{A} & \text{on } \mathcal{I} \times [0,T], \end{cases} \tag{13}$$

where $\mathcal{A}$ denotes the set of physically admissible states (ψ, h). The admissible set $\mathcal{A}$ (see Figure 2) has two branches, the branch $\{h = 0\}$ is associated with the dry surface where the soil hydraulic head is less than or equal to zero corresponding to unsaturated conditions, while the branch $\{h = \psi\}$ is associated with the wet surface where the soil is saturated and the hydraulic head is in hydrostatic equilibrium with the overland flow pressure. Thus, the admissible set $\mathcal{A}$ is defined as

$$\mathcal{A} \stackrel{\text{def}}{=} \{(\psi, h) \in \mathbb{R}^2,\ h = \psi^+\}, \tag{14}$$

where $\psi^+ = \frac{1}{2}(\psi + |\psi|)$ is the positive part of ψ.

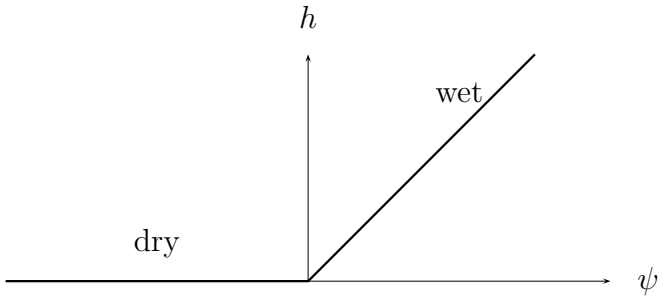

Figure 2. The admissible set $\mathcal{A}$.

We mainly focus here on situations where the overland flow is produced by exfiltration. Indeed in this situation, a smooth behavior on the admissible set can be expected. More drastic situations like runon surface waves on unsaturated soils can in many cases lead to a departure from the admissible set especially if the soil is too dry. In these limit situations, other models can be more suitable: for instance when infiltration processes are very slow, a model where surface flow coexists with an unsaturated soil can be envisaged.

3 Discretization

3.1 Discretization of Richards' equation

Let $\{\mathcal{T}_\mathfrak{h}\}_{\mathfrak{h}>0}$ be a shape-regular family of unstructured meshes of Ω consisting for simplicity of affine triangles. The meshes can possess hanging nodes. For an element $\tau \in \mathcal{T}_\mathfrak{h}$, let $\partial\tau$ denote its boundary and n_τ its outward unit normal. The discontinuous finite element space $V_\mathfrak{h}$ is defined as

$$V_\mathfrak{h} \stackrel{\text{def}}{=} \{\phi \in L^2(\Omega),\ \forall \tau \in \mathcal{T}_\mathfrak{h},\ \phi|_\tau \in \mathbb{P}_p(\tau)\}, \tag{15}$$

where $\mathbb{P}_p(\tau)$ is the set of polynomials of total degree less than or equal to p on an element τ. We observe that the functions in $V_\mathfrak{h}$ need not be continuous. This fact is exploited by selecting basis functions which are locally supported in a single mesh element. The set $\mathcal{F}_\mathfrak{h}$ of mesh faces is partitioned into $\mathcal{F}_\mathfrak{h}^\mathrm{i} \cup \mathcal{F}_\mathfrak{h}^{\mathcal{WB}} \cup \mathcal{F}_\mathfrak{h}^{\mathcal{I}}$ where $\mathcal{F}_\mathfrak{h}^\mathrm{i}$ is the set of internal faces, $\mathcal{F}_\mathfrak{h}^{\mathcal{WB}}$ the set of faces located on $\mathcal{W} \cup \mathcal{B}$, and $\mathcal{F}_\mathfrak{h}^{\mathcal{I}}$ the set of faces located on $\mathcal{I}$. For a face $F \in \mathcal{F}_\mathfrak{h}^\mathrm{i}$, there are τ^+ and τ^- in $\mathcal{T}_\mathfrak{h}$ such that $F = \partial\tau^+ \cap \partial\tau^-$ and we define the average operator $\{\}_F$ and the jump operator $[\![]\!]_F$ as follows: for a function ξ which is possibly two-valued on F,

$$\{\xi\}_F \stackrel{\text{def}}{=} \frac{1}{2}(\xi^+ + \xi^-) \quad \text{and} \quad [\![\xi]\!]_F \stackrel{\text{def}}{=} \xi^- - \xi^+,$$

where $\xi^\pm = \xi|_{\tau^\pm}$. For vector-valued functions, average and jump operators are defined componentwise. We define n_F to be the unit normal vector to F pointing from τ^- to τ^+. The arbitrariness in the sign of the jump is irrelevant in the sequel.

In the present work, faces on $\mathcal{I}$ can exclusively be flagged either as dry or as wet, that is, we do not track the wet/dry interface inside such faces. As a result, the set $\mathcal{F}_\mathfrak{h}^{\mathcal{I}}$ can be further divided into $\mathcal{F}_\mathfrak{h}^{\mathrm{d},t}$ and $\mathcal{F}_\mathfrak{h}^{\mathrm{w},t}$, where $\mathcal{F}_\mathfrak{h}^{\mathrm{d},t}$ collects the faces flagged as dry and $\mathcal{F}_\mathfrak{h}^{\mathrm{w},t}$ those flagged as wet. These two sets of faces induce a partition of $\mathcal{I}$ as $\mathcal{I}_\mathfrak{h}^{\mathrm{d},t} \cup \mathcal{I}_\mathfrak{h}^{\mathrm{w},t}$, where

$$\mathcal{I}_\mathfrak{h}^{\mathrm{d},t} \stackrel{\text{def}}{=} \{x \in \mathcal{I},\ \exists F \in \mathcal{F}_\mathfrak{h}^{\mathrm{d},t},\ x \in F\} \text{ and } \mathcal{I}_\mathfrak{h}^{\mathrm{w},t} \stackrel{\text{def}}{=} \{x \in \mathcal{I},\ \exists F \in \mathcal{F}_\mathfrak{h}^{\mathrm{w},t},\ x \in F\}.$$

Space discretization

Let $\psi_\mathfrak{h}$ be the discrete approximation of ψ. The symmetric interior penalty discontinuous Galerkin method for Richards' equation can be concisely written as

$$\forall \tau \in \mathcal{T}_\mathfrak{h}, \quad \forall \phi \in \mathbb{P}_p(\tau), \quad \int_\tau \partial_t[\theta(\psi_\mathfrak{h})]\phi + a_\tau(\psi_\mathfrak{h}, \phi) = b_\tau(\psi_\mathfrak{h}, \phi), \tag{16}$$

where for $(\psi,\phi)\in V_{\mathfrak{h}}\times\mathbb{P}_p(\tau)$,

$$a_\tau(\psi,\phi)\stackrel{\rm def}{=}\int_\tau K(\psi)\nabla\psi\cdot\nabla\phi+\int_{\partial\tau}K(\psi)\ \nabla\phi\cdot n_\tau\ (\widehat{\psi}(\psi)-\psi)+\int_{\partial\tau}\widehat{u}(\psi)\cdot n_\tau\ \phi,$$
$$b_\tau(\psi,\phi)\stackrel{\rm def}{=}\int_\tau\nabla\cdot(K(\psi)\nabla z)\ \phi+\tilde{b}_\tau(\psi,\phi).$$

Here, $\widehat{\psi}(\psi)$ is the numerical flux associated with the hydraulic head

$$\forall F\in\mathcal{F}_{\mathfrak{h}},\ \widehat{\psi}(\psi)|_F\stackrel{\rm def}{=}\begin{cases}\{\psi\}_F & \text{if } F\in\mathcal{F}_{\mathfrak{h}}^{\rm i},\\ 0 & \text{if } F\in\mathcal{F}_{\mathfrak{h}}^{{\rm w},t},\\ \psi & \text{if } F\in\mathcal{F}_{\mathfrak{h}}^{{\rm d},t}\cup\mathcal{F}_{\mathfrak{h}}^{\mathcal{WB}},\end{cases}$$

and $\widehat{u}(\psi)$ is the numerical flux associated with $u\stackrel{\rm def}{=}-K(\psi)\nabla\psi$,

$$\forall F\in\mathcal{F}_{\mathfrak{h}},\ \widehat{u}(\psi)|_F\stackrel{\rm def}{=}\begin{cases}-\{K(\psi)\nabla\psi\}_F+\eta K_s d_F^{-1}[\![\psi]\!]_F n_F & \text{if } F\in\mathcal{F}_{\mathfrak{h}}^{\rm i},\\ -\ K(\psi)\nabla\psi+\eta K_s d_F^{-1}\psi n_\Omega & \text{if } F\in\mathcal{F}_{\mathfrak{h}}^{{\rm w},t},\\ 0 & \text{if } F\in\mathcal{F}_{\mathfrak{h}}^{{\rm d},t}\cup\mathcal{F}_{\mathfrak{h}}^{\mathcal{WB}},\end{cases}$$

where η is a positive parameter (to be taken larger than a minimal threshold depending on the shape-regularity of $\mathcal{T}_{\mathfrak{h}}$), K_s the hydraulic conductivity at saturation, and d_F is defined as the largest diameter of the triangle(s) of which F is a face. Observe that for a flow in a porous medium with variable conductivity (as in variably saturated flows because of the dependence of the conductivity on the hydraulic head), the penalty coefficient at a given interface should scale as the harmonic means of the normal hydraulic conductivity on both parts of the interface, see [12,15]. Here, the variations of K are sufficiently mild to use simply the hydraulic conductivity at saturation. Furthermore,

$$\tilde{b}_\tau(\psi,\phi)\stackrel{\rm def}{=}\int_{\partial\tau\cap\mathcal{F}_{\mathfrak{h}}^{{\rm w},t}}\Big(-K(\psi)\ \nabla\phi\cdot n_\Omega\ +\eta K_s d_F^{-1}\phi\Big)\omega_\psi$$
$$-\int_{\partial\tau\cap\mathcal{F}_{\mathfrak{h}}^{{\rm d},t}}(\omega_v+K(\psi)\nabla z\cdot n_\Omega)\phi-\int_{\partial\tau\cap\mathcal{F}_{\mathfrak{h}}^{\mathcal{WB}}}(v_N+K(\psi)\nabla z\cdot n_\Omega)\phi.$$

Summing $a_\tau(\psi,\phi)$ over all mesh elements yields the global form

$$a_{\mathfrak{h}}(\psi,\phi)=\sum_{\tau\in\mathcal{T}_{\mathfrak{h}}}\int_\tau K(\psi)\nabla\psi\cdot\nabla\phi$$
$$-\sum_{F\in\mathcal{F}_{\mathfrak{h}}^{\rm i}}\int_F\Big(\{K(\psi)\nabla\phi\}_F[\![\psi]\!]_F\cdot n_F+\{K(\psi)\nabla\psi\}_F[\![\phi]\!]_F\cdot n_F-\eta K_s d_F^{-1}[\![\psi]\!]_F[\![\phi]\!]_F\Big)$$
$$-\sum_{F\in\mathcal{F}_{\mathfrak{h}}^{{\rm w},t}}\int_F\Big(K(\psi)\nabla\phi\ \psi\cdot n_F+K(\psi)\nabla\psi\ \phi\cdot n_F-\eta K_s d_F^{-1}\psi\phi\Big).\qquad(17)$$

The parameter η must be chosen large enough to ensure that the form $a_{\mathfrak{h}}$ is coercive, in the sense that there is $\alpha > 0$ such that for all $\phi \in V_{\mathfrak{h}}$,

$$a_{\mathfrak{h}}(\phi,\phi) \geq \alpha\Big(\sum_{\tau\in\mathcal{T}_{\mathfrak{h}}} \int_\tau K(\phi)|\nabla\phi|^2 + \sum_{F\in\mathcal{F}_{\mathfrak{h}}^{\mathrm{i}}} K_s d_F^{-1} \int_F [\![\phi]\!]^2 + \sum_{F\in\mathcal{F}_{\mathfrak{h}}^{\mathrm{w},t}} K_s d_F^{-1} \int_F \phi^2 \Big).$$

Time discretization

Let N_T be the total number of time steps and let δt be the time step taken to be constant for simplicity and such that $N_T \stackrel{\text{def}}{=} T/\delta t$ is an integer. For any function of time χ and for any integer $n \geq 0$, χ^n denotes the value taken by χ at the discrete time $n\delta t$. Furthermore, the time derivative of $\chi \in C^{q+1}$ can be approximated by a backward differentiation formula [27] in the form

$$(\partial_t\chi)^n = \sum_{r=0}^{q} \frac{\alpha_r^q}{\delta t}\chi^{n-r} + \mathcal{O}(\delta t^q), \tag{18}$$

where q is the order of the formula and $\{\alpha_r^q\}_{0\leq r\leq q}$ are suitable coefficients. Using the approximation (18) in (16) for each $n \in \{1\cdots N_T\}$ leads to

$$\begin{aligned} &\forall\tau\in\mathcal{T}_{\mathfrak{h}}, \quad \forall\phi\in\mathbb{P}_p(\tau),\\ &\quad \frac{\alpha_0^q}{\delta t}\int_\tau \theta(\psi_{\mathfrak{h}}^n)\phi + a_\tau(\psi_{\mathfrak{h}}^n,\phi) = b_\tau(\psi_{\mathfrak{h}}^n,\phi) - \sum_{r=1}^{q}\frac{\alpha_r^q}{\delta t}\int_\tau \theta(\psi_{\mathfrak{h}}^{n-r})\phi. \end{aligned} \tag{19}$$

For the first few time steps, a BDF of lower order or a one-step implicit scheme can be used, for example a diagonally implicit Runge–Kutta scheme or the Crank–Nicolson scheme. The former presents the drawback that the last step requires solving a nonlinear problem of the form (19), but without the contribution of the form a_τ in the left-hand side. Thus, if the soil is at least partially saturated, this problem becomes ill-posed.

Nonlinear iterative solver

The nonlinear equation (19) is solved by a quasi-Newton method where the dependence of K on ψ is treated explicitly. Hence, we add a third argument to the form a_τ and for all $\forall\ (\zeta,\psi,\phi) \in V_{\mathfrak{h}}\times V_{\mathfrak{h}}\times\mathbb{P}_p(\tau)$, we define

$$\widehat{a}_\tau(\zeta,\psi,\phi) \stackrel{\text{def}}{=} \int_\tau K(\zeta)\nabla\psi\cdot\nabla\phi + \int_{\partial\tau} K(\zeta|_\tau)\,\nabla\phi\cdot n_\tau\,(\widehat{\mathrm{F}}_\psi(\psi)-\psi) + \int_{\partial\tau}\widehat{\mathrm{F}}_u(\zeta,\psi)\cdot n_\tau\,\phi,$$

with the flux $\widehat{\mathrm{F}}_u(\zeta,\psi)$ given by

$$\forall F\in\mathcal{F}_{\mathfrak{h}},\ \widehat{\mathrm{F}}_u(\zeta,\psi)|_F \stackrel{\text{def}}{=} \begin{cases} -\{K(\zeta)\nabla\psi\}_F+\eta K_{\mathrm{s}}d_F^{-1}[\![\psi]\!]_F n_F & \text{if } F\in\mathcal{F}_{\mathfrak{h}}^{\mathrm{i}},\\ -\ K(\zeta)\nabla\psi+\eta K_{\mathrm{s}}d_F^{-1}\psi n_\Omega & \text{if } F\in\mathcal{F}_{\mathfrak{h}}^{\mathrm{w},t},\\ 0 & \text{if } F\in\mathcal{F}_{\mathfrak{h}}^{\mathrm{d},t}\cup\mathcal{F}_{\mathfrak{h}}^{\mathcal{WB}}. \end{cases}$$

The discrete functions $\left\{\psi_{\mathfrak{h}}^{n-r}\right\}_{1\le r\le q}$ being known, successive approximations $\psi_{\mathfrak{h}}^{n,m}$ of $\psi_{\mathfrak{h}}^{n}$ are computed from

$$\begin{aligned}\forall\tau\in\mathcal{T}_{\mathfrak{h}},\ \forall\phi\in\mathbb{P}_p(\tau),\ \frac{\alpha_0^q}{\delta t}\int_\tau\Big(\theta(\psi_{\mathfrak{h}}^{n,m})+\partial_\psi\theta(\psi_{\mathfrak{h}}^{n,m})(\psi_{\mathfrak{h}}^{n,m+1}-\psi_{\mathfrak{h}}^{n,m})\Big)\phi\\ +\ \widehat{a}_\tau(\psi_{\mathfrak{h}}^{n,m},\psi_{\mathfrak{h}}^{n,m+1},\phi)=b_\tau(\psi_{\mathfrak{h}}^{n,m},\phi)-\sum_{r=1}^{q}\frac{\alpha_r^q}{\delta t}\int_\tau\theta(\psi_{\mathfrak{h}}^{n-r})\phi.\end{aligned}\tag{20}$$

Let $\delta\psi_{\mathfrak{h}}^{n,m}=\psi_{\mathfrak{h}}^{n,m+1}-\psi_{\mathfrak{h}}^{n,m}$ and let d_τ be defined as $d_\tau(\zeta,\psi,\phi)\stackrel{\text{def}}{=}\displaystyle\int_\tau\partial_\psi\theta(\zeta)\psi\phi$, so that equation (20) can be written as

$$\begin{aligned}&\forall\tau\in\mathcal{T}_{\mathfrak{h}},\quad\forall\phi\in\mathbb{P}_p(\tau),\\ &\frac{\alpha_0^q}{\delta t}d_\tau(\psi_{\mathfrak{h}}^{n,m},\delta\psi_{\mathfrak{h}}^{n,m},\phi)+\widehat{a}_\tau(\psi_{\mathfrak{h}}^{n,m},\delta\psi_{\mathfrak{h}}^{n,m},\phi)=b_\tau(\psi_{\mathfrak{h}}^{n,m},\phi)\\ &\quad-\sum_{r=1}^{q}\frac{\alpha_r^q}{\delta t}\int_\tau\theta(\psi_{\mathfrak{h}}^{n-r})\phi-\frac{\alpha_0^q}{\delta t}\int_\tau\theta(\psi_{\mathfrak{h}}^{n,m})\phi-\widehat{a}_\tau(\psi_{\mathfrak{h}}^{n,m},\psi_{\mathfrak{h}}^{n,m},\phi).\end{aligned}\tag{21}$$

Algorithm 1 Quasi-Newton method for solving Richards' equation

Input: $\psi_{\mathfrak{h}}^{n-1},\psi_{\mathfrak{h}}^{n-2},\cdots,\psi_{\mathfrak{h}}^{n-q},\psi_{\mathfrak{h}}^{n,0},\epsilon_{alg1}$
  set $m=0$
  repeat
    Find $\delta\psi_{\mathfrak{h}}^{n,m}\in V_{\mathfrak{h}}$ solving (21)
    set $\psi_{\mathfrak{h}}^{n,m+1}=\psi_{\mathfrak{h}}^{n,m}+\delta\psi_{\mathfrak{h}}^{n,m}$
    $m\leftarrow m+1$
  until $E\le\epsilon_{alg1}$
Output: $\psi_{\mathfrak{h}}^{n}=\psi_{\mathfrak{h}}^{n,m}$

The simplest initialization of Algorithm 1 consisting in choosing the approximation of the solution at the previous time step ($\psi_{\mathfrak{h}}^{n,0}=\psi_{\mathfrak{h}}^{n-1}$), but a higher order initialization can also be used (see §4). The error measure E is the relative Euclidean norm of the component vector associated with $\delta\psi_{\mathfrak{h}}^{n,m}$, and ϵ_{alg1} is a user-defined convergence criterion.

The kinematic wave equation is discretized on a surface mesh on $\mathcal{I}$ which is simply the trace of the mesh $\mathcal{T}_\mathfrak{h}$ on $\mathcal{I}$. Let $N_\mathcal{I}$ be the number of mesh faces covering $\mathcal{I}$. Spatial discretization is based on a finite volume scheme with Godunov flux, that is, first-order upwinding. This choice is made for the sake of simplicity, but using a finite volume scheme with second-order reconstruction and limiting is also possible. The time step $\delta t'$ in the finite volume scheme is taken less than or equal to the time step for Richards' equation, and more specifically in the form $\delta t' = \delta t/n'$ with $n' \geq 1$ (see Figure 3). This choice is made because the explicit FV scheme is, as usual, restricted by a CFL condition to ensure its stability. This is not the case for the discrete Richards' equation where, owing to the use of a BDF, a larger time step can be employed. This leads to the following notation: $h_\mathfrak{h}^{n,k}$ for $n \in \{1 \cdots N_T\}$ and $k \in \{0 \cdots n'\}$ denotes the discrete approximation of h at time $n\delta t + k\delta t'$ and for brevity we write $h_\mathfrak{h}^n \stackrel{\text{def}}{=} h_\mathfrak{h}^{n,0} = h_\mathfrak{h}^{n-1,n'}$. Let x_i, l_i, $x_{i-\frac{1}{2}}$ and $x_{i+\frac{1}{2}}$ be defined on a generic

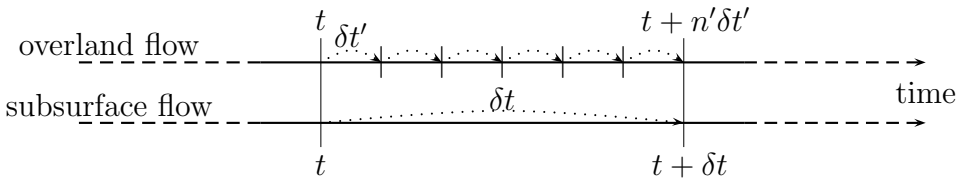

Figure 3. Multiple time-stepping for subsurface and overland flows.

mesh face e_i on $\mathcal{I}$ respectively as the center, the length, and the left and right vertices of e_i (see Figure 4). S_i denotes the slope of the face e_i. Since the flux function φ is convex and the surface water depth is nonnegative, the Godunov flux coincides with the upwind flux, yielding $\forall k \in \{1 \cdots n'\},\ \forall i \in \{1 \cdots N_\mathcal{I}\}$,

$$h_i^{n-1,k} = h_i^{n-1,k-1} + \frac{\delta t'}{l_i}\Big(\varphi(h_{i-1}^{n-1,k-1}, S_{i-1}) - \varphi(h_i^{n-1,k-1}, S_i)\Big) - \delta t' v_\mathrm{r}^{n-1,k-1} \cdot n_\Omega + \frac{\delta t'}{l_i}\int_{e_i} v_\mathfrak{h}^{\star,n}, \tag{22}$$

where for all $i \in \{1 \cdots N_\mathcal{I}\}$, $h_i^{n,k} \stackrel{\text{def}}{=} h_\mathfrak{h}^{n,k}|_{e_i}$ and $v_\mathfrak{h}^{\star,n}$ is a discrete interface flux yet to be defined (see §3.3). Observe that a fixed interface flux is used for the multiple time steps comprised in a single time step of Richards' equation. Equation (22) requires the knowledge of the surface water depth at $t = 0$ (initial condition) and to the left of the first face on a fictitious cell (boundary condition) at all discrete times, $\forall i \in \{1 \cdots N_\mathcal{I}\}$, $h_i^0 = h^0(x_i)$ and $\forall n \in \{1 \cdots N_T\}, \forall k \in \{0 \cdots n' - 1\}$, $h_{-1}^{n,k} = h_\mathrm{A}^{n,k}$.

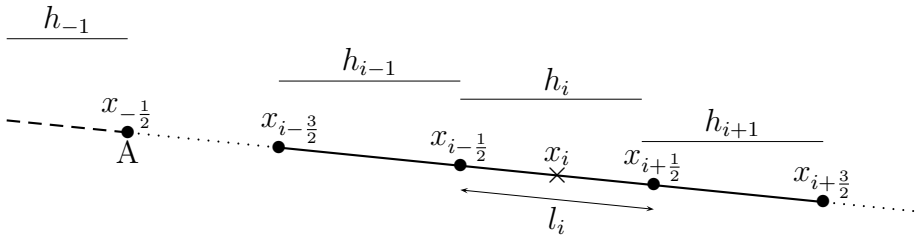

Figure 4. Space discretization at the ground surface.

The CFL condition for the explicit scheme (22) can be expressed as

$$\delta t' \leq \min_{1\leq i\leq N_{\mathcal{I}}} \Big(\frac{l_i}{\partial_h \varphi(h_{\max}, S_i)}\Big), \tag{23}$$

where $h_{\max}$ is an *a priori* bound for the surface surface water depth h on $\mathcal{I}\times[0,T]$. By definition of the flux function φ, this yields

$$\delta t' \leq \frac{3}{5\mathcal{K}h_{\max}^{2/3}} \cdot \min_{1\leq i\leq N_{\mathcal{I}}} \Big(l_i S_i^{-\frac{1}{2}}\Big).$$

In the absence of rainfall and coupling terms, the satisfaction of the CFL condition implies a discrete maximum principle and a decrease in the total variation for the discrete surface water depth.

3.3 Single-step coupling algorithm

We consider in this section the case where Richards' equation is discretized in time using a first-order BDF (that is, the Euler implicit scheme). Together with the finite volume scheme described in §3.2 for the kinematic wave equation, this yields a scheme to approximate the coupled system (13) provided we specify the time evolution of the coupling variables $\{\mathcal{I}_{\mathfrak{h}}^{\mathrm{d},n}, \mathcal{I}_{\mathfrak{h}}^{\mathrm{w},n}, \omega_v^n, \omega_\psi^n\}$ for $n\in\{1\cdots N_T\}$ (see §2.4). Here, as before, the superscript n stands for the value at $n\delta t$, so that $\mathcal{I}_{\mathfrak{h}}^{\mathrm{d},n} = \mathcal{I}_{\mathfrak{h}}^{\mathrm{d},n\delta t}$ and so on. This time evolution is designed with the twofold objective to ensure that a suitable approximation of (ψ,h) lies in the admissible set $\mathcal{A}$ at all discrete times and to ensure overall mass conservation for the whole system (subsurface and overland flows). The resulting algorithm is outlined in Algorithm 2. It is termed single-step coupling algorithm in reference to the use of the first-order BDF which spans a single time step interval. For simplicity in the presentation of Algorithm 2, we define

- $\psi_{\mathfrak{h}}^n \leftarrow$ `Richards_BDF1`$(\mathcal{I}_{\mathfrak{h}}^{\mathrm{d},n}, \mathcal{I}_{\mathfrak{h}}^{\mathrm{w},n}, \omega_v^n, \omega_\psi^n, \psi_{\mathfrak{h}}^{n-1})$ as the resolution by Algorithm 1 of Richards' equation on a time step by the SIPG method, the first-order BDF and boundary data on $\mathcal{I}$ determined from $\{\mathcal{I}_{\mathfrak{h}}^{\mathrm{d},n}, \mathcal{I}_{\mathfrak{h}}^{\mathrm{w},n}, \omega_v^n, \omega_\psi^n\}$,
- $h_{\mathfrak{h}}^n \leftarrow$ `Kinematic_wave`$(h_{\mathfrak{h}}^{n-1}, n', v_{\mathrm{r}}, v_{\mathfrak{h}}^{\star,n})$ as the resolution of the kinematic wave equation by using (22) n' times,

- $v_\mathfrak{h}^{\star,n} \leftarrow$ `Normal_Velocity`$(\mathcal{I}_\mathfrak{h}^{\mathrm{d},n}, \mathcal{I}_\mathfrak{h}^{\mathrm{w},n}, \omega_v^n, \omega_\psi^n, \psi_\mathfrak{h}^n)$ as the evaluation of the interface normal velocity $v_\mathfrak{h}^{\star,n}$ on $\mathcal{I}$ defined as

$$v_\mathfrak{h}^{\star,n}|_F \stackrel{\text{def}}{=} \begin{cases} \omega_v^n|_F & \text{if } F \in \mathcal{I}_\mathfrak{h}^{\mathrm{d},n}, \\ v(\psi_\mathfrak{h}^n|_F) \cdot n_\Omega + \eta K_s d_F^{-1}(\psi_\mathfrak{h}^n|_F - \omega_\psi^n|_F) & \text{if } F \in \mathcal{I}_\mathfrak{h}^{\mathrm{w},n}. \end{cases} \tag{24}$$

  Note that the expression for $v_\mathfrak{h}^{\star,n}$ on $\mathcal{I}_\mathfrak{h}^{\mathrm{w},n}$ corresponds to the normal component of the $H(\mathrm{div},\Omega)$-conforming velocity reconstruction derived in [14] for DG methods.

Algorithm 2 Single-step coupling algorithm

Input: $\psi_\mathfrak{h}^{n-1}$ and $h_\mathfrak{h}^{n-1}$

$\tilde{h}_\mathfrak{h}^n \leftarrow$`Kinematic_wave`$(h_\mathfrak{h}^{n-1}, n', v_\mathrm{r}^{n-1}, 0)$

Set $p = 0$ and $h_\mathfrak{h}^{n,0} = \tilde{h}_\mathfrak{h}^n$

repeat

$p \leftarrow p + 1$

$\mathcal{I}_\mathfrak{h}^{\mathrm{d},n,p} = \{e_i \in \mathcal{I}_\mathfrak{h}, \exists k \in \{0 \cdots p-1\}, h_i^{n,k} < 0\}$ and $\mathcal{I}_\mathfrak{h}^{\mathrm{w},n,p} = \mathcal{I} \backslash \mathcal{I}_\mathfrak{h}^{\mathrm{d},n,p}$

$\omega_v^{n,p} \leftarrow -\tilde{h}_\mathfrak{h}^n/\delta t$ on $\mathcal{I}_\mathfrak{h}^{\mathrm{d},n,p}$

$\omega_\psi^{n,p} \leftarrow \tilde{h}_\mathfrak{h}^n$ on $\mathcal{I}_\mathfrak{h}^{\mathrm{w},n,p}$

$\psi_\mathfrak{h}^{n,p} \leftarrow$ `Richards_BDF1`$(\mathcal{I}_\mathfrak{h}^{\mathrm{d},n,p}, \mathcal{I}_\mathfrak{h}^{\mathrm{w},n,p}, \omega_v^{n,p}, \omega_\psi^{n,p}, \psi_\mathfrak{h}^{n-1})$

$v_\mathfrak{h}^{\star,n,p} \leftarrow$ `Normal_Velocity`$(\mathcal{I}_\mathfrak{h}^{\mathrm{d},n,p}, \mathcal{I}_\mathfrak{h}^{\mathrm{w},n,p}, \omega_v^{n,p}, \omega_\psi^{n,p}, \psi_\mathfrak{h}^{n,p})$

$\forall i \in \{1 \cdots N_\mathcal{I}\}, h_i^{n,p} = \tilde{h}_i^n + \delta t/l_i \int_{e_i} v_\mathfrak{h}^{\star,n,p}$

until $\forall\, i \in \{1 \cdots N_\mathcal{I}\}, h_i^{n,p} \geq 0$

Output: $\psi_\mathfrak{h}^n = \psi_\mathfrak{h}^{n,p}$ and $h_\mathfrak{h}^n = h_\mathfrak{h}^{n,p}$

The principle of Algorithm 2 is the following. Firstly, the surface water depth is predicted without subsurface coupling term ($v_\mathfrak{h}^{\star,n} = 0$). This predicted surface water depth $\tilde{h}_\mathfrak{h}^n$ then serves as a Dirichlet boundary condition for Richards' equation. Because the Godunov scheme satisfies a discrete maximum principle, $\tilde{h}_i^n \geq 0$ for all $i \in \{1 \cdots N_\mathcal{I}\}$, so that $\mathcal{I}_\mathfrak{h}^{\mathrm{d},n,1} = \emptyset$ and $\mathcal{I}_\mathfrak{h}^{\mathrm{w},n,1} = \mathcal{I}$. That is, we begin the iterations by assuming that $\mathcal{I}$ is totally wet. Thus, for $p = 1$, the determination of $\omega_v^{n,p}$ is irrelevant. Then, Richards' equation is solved and a first estimate of the normal velocity $v_\mathfrak{h}^{\star,n,p}$ is used to evaluate the surface water depth $h_\mathfrak{h}^{n,p}$. The sign of $h_\mathfrak{h}^{n,p}$ is subsequently checked on the faces of $\mathcal{I}$. If $h_\mathfrak{h}^{n,p}$ is nonnegative on all faces, the evaluation of the hydraulic head and of the surface water depth can be accepted as the solution to the coupled system at time $n\delta t$. Otherwise, a new partition of $\mathcal{I}$ is determined and a Neumann condition is enforced on those faces where the surface water depth is negative. This Neumann condition is evaluated in such a way that at the corresponding

interface cells, the surface water is completely infiltrated into the soil since $\omega_v^{n,p} = -\tilde{h}_\mathfrak{h}^n/\delta t$. A new hydraulic head and a new surface water depth are then calculated and the loop is repeated until convergence. Note that convergence occurs since the set $\mathcal{I}_\mathfrak{h}^{\mathrm{d},n,p}$ increases with p while the set $\mathcal{I}_\mathfrak{h}^{\mathrm{w},n,p}$ decreases.

Admissibility of (ψ, h)

An important point is that Algorithm 2 delivers nonnegative surface water depths. Moreover, on the wet part of the interface, there holds

$$\forall n \in \{1 \cdots N_T\}, \quad \forall F \in \mathcal{I}_\mathfrak{h}^{\mathrm{w},n}, \quad \psi_\mathfrak{h}^n|_F = \tilde{h}_\mathfrak{h}^n|_F,$$

since the value of the Dirichlet data $\omega_\psi^{n,p}$ on $\mathcal{I}_\mathfrak{h}^{\mathrm{w},n,p}$ is fixed during the loop. This is not the condition $\psi = h$ enforced by the admissible set $\mathcal{A}$ but an $\mathcal{O}(\delta t)$ approximation of it. Furthermore, on the dry part of the interface, the surface water depth is equal to zero and it is reasonable to expect that

$$\forall n \in \{1 \cdots N_T\}, \quad \forall F \in \mathcal{I}_\mathfrak{h}^{\mathrm{d},n}, \quad \psi_\mathfrak{h}^n|_F \leq \tilde{h}_\mathfrak{h}^n|_F.$$

Indeed, the coupling algorithm starts by enforcing $\tilde{h}_\mathfrak{h}^n$ as Dirichlet boundary value for $\psi_\mathfrak{h}^n$ everywhere on the interface. If a face becomes dry, this means that the infiltration flux must be reduced; therefore, $\psi_\mathfrak{h}^n$ can be expected to diminish and thus to stay below $\tilde{h}_\mathfrak{h}^n$. Moreover, on a face that has become dry, smooth behavior in time yields that $\tilde{h}_\mathfrak{h}^n$ is $\mathcal{O}(\delta t)$. As a result, we expect to recover an $\mathcal{O}(\delta t)$ approximation of the condition $\psi \leq 0$ enforced by the admissible set. Numerical experiments confirm that ψ does not exceed small positive values in dry areas.

In addition, we observe that, if on a given face e_i, the surface water depth h_i^{n-1} is zero as well as the upwind fluxes over the time step $[(n-1)\delta t, n\delta t]$, the Neumann condition on Richards' equation is equal to the rainfall intensity. Moreover, we observe that in contrast to front tracking schemes, Algorithm 2 does not use any information from the previous time step to determine the wet portion of the interface. This offers the advantage of robustness and ease of extension to 3D/2D settings, but can entail higher computational costs than those incurred by front tracking schemes in the absence of exfiltration (see for instance [7]).

Overall mass conservation

The total volume of water in the domain Ω at time $n\delta t$ is obtained by integrating the volumetric water content in Ω

$$V_{\mathrm{grnd}}^n \stackrel{\mathrm{def}}{=} \int_\Omega \theta(\psi_\mathfrak{h}^n).$$

Taking the test function ϕ equal to 1 in the SIPG scheme (21), summing over the mesh elements and using the first-order BDF to approximate the non-stationary term yields

$$V_{\rm grnd}^n - V_{\rm grnd}^{n-1} = \Big(F_{\mathcal{I}}^n + F_{\mathcal{WB}}^n\Big)\delta t + \epsilon^n, \tag{25}$$

where $F_{\mathcal{I}}^n$ (resp. $F_{\mathcal{WB}}^n$) is the flux over the time step $[(n-1)\delta t, n\delta t]$ across the interface $\mathcal{I}$ (resp. across the bottom and lateral walls),

$$F_{\mathcal{I}}^n \stackrel{\rm def}{=} -\int_{\mathcal{I}} v_{\mathfrak{h}}^{\star,n} \quad \text{and} \quad F_{\mathcal{WB}}^n \stackrel{\rm def}{=} -\int_{\mathcal{W}\cup\mathcal{B}} v_N^n, \tag{26}$$

and ϵ^n represents the numerical error in the resolution of the nonlinear system. Recall that $|\epsilon^n| \leq C\epsilon_{alg1}$, where ϵ_{alg1} is the convergence tolerance of Algorithm 1 and C a constant due to the fact that the convergence criterion in Algorithm 1 limits the norm of the variation of the hydraulic head ψ rather than the one of the volumetric water content $\theta(\psi)$. The total volume of water in the overland flow at time $n\delta t$ is obtained by integrating the surface water depth over $\mathcal{I}$

$$V_{\rm over}^n \stackrel{\rm def}{=} \int_{\mathcal{I}} h_{\mathfrak{h}}^n.$$

The variation of the total volume of water in the overland flow over the time step $[(n-1)\delta t, n\delta t]$ is obtained by summing the elementary contributions in equation (22), yielding

$$V_{\rm over}^n - V_{\rm over}^{n-1} = \Big(-F_{\mathcal{I}}^n + F_{\rm ABr}^n\Big)\delta t, \tag{27}$$

where $F_{\mathcal{I}}^n$ is already defined above and where $F_{\rm ABr}^n$ represents the water flux over the time step $[(n-1)\delta t, n\delta t]$ due to the rain and the discharge at points A and B, with $F_{\rm ABr}^n \stackrel{\rm def}{=} F_{\rm A}^n + F_{\rm B}^n + F_{\rm r}^n$, and

$$F_{\rm A}^n \stackrel{\rm def}{=} \frac{\delta t'}{\delta t}\sum_{k=1}^{n'} \varphi(h_{\rm A}^{n-1,k}),\ F_{\rm B}^n \stackrel{\rm def}{=} -\frac{\delta t'}{\delta t}\sum_{k=1}^{n'} \varphi(h_{N_{\mathcal{I}}}^{n-1,k}),\ F_{\rm r}^n \stackrel{\rm def}{=} -\frac{\delta t'}{\delta t}\sum_{k=1}^{n'}\int_{\mathcal{I}} v_{\rm r}^{n-1,k}\cdot n_\Omega.$$

The total volume of water contained in the coupled system is the sum of the volume of each system, $V^n \stackrel{\rm def}{=} V_{\rm grnd}^n + V_{\rm over}^n$. When (25) and (27) are summed, the interface flux cancels, yielding

$$V^n - V^{n-1} = \Big(F_{\mathcal{WB}}^n + F_{\rm ABr}^n\Big)\delta t + \epsilon^n. \tag{28}$$

This relation readily implies the following overall water volume conservation result for the single-step algorithm.

Property 1 *Let δV^n be the overall water volume defect over the time step $[(n-1)\delta t, n\delta t]$ defined as $\delta V^n \stackrel{\rm def}{=} V^n - V^{n-1} - (F_{\mathcal{WB}}^n + F_{\rm ABr}^n)\delta t$. Let $\triangle V^n$ be the overall water volume defect over the time interval $[0, n\delta t]$ defined as $\triangle V^n \stackrel{\rm def}{=} \sum_{i=1}^n \delta V^i$. Then,*

$$|\triangle V^n| \leq nC\epsilon_{alg1}, \tag{29}$$

where C is a constant and ϵ_{alg1} is the tolerance in Algorithm 1.

3.4 Two-step coupling algorithm

We consider in this section the case where Richards' equation is discretized in time using a second-order BDF for which

$$\Big(\frac{\partial\chi}{\partial t}\Big)^n \simeq \frac{1}{\delta t}\Big(\frac{3}{2}\chi^n - 2\chi^{n-1} + \frac{1}{2}\chi^{n-2}\Big). \tag{30}$$

The single-step coupling algorithm is not conservative when the non-stationary term of Richards' equation is approximated by the second-order BDF owing to the fact that the Euler explicit scheme used to solve the kinematic wave equation spans only a single time step. Consequently, to obtain a mass conservative scheme, the interface flux $F_{\mathcal{I}}^n$ used in the kinematic wave equation needs to be transformed into a new interface flux $\Phi_{\mathcal{I}}^n$, so that (27) becomes

$$V_{\rm over}^n - V_{\rm over}^{n-1} = \Big(- \Phi_{\mathcal{I}}^n + F_{\rm ABr}^n\Big)\delta t. \tag{31}$$

To identify the expression for $\Phi_{\mathcal{I}}^n$, observe that using a second-order BDF modifies (25) into

$$\frac{3}{2}V_{\rm grnd}^n - 2V_{\rm grnd}^{n-1} + \frac{1}{2}V_{\rm grnd}^{n-2} = \Big(F_{\mathcal{I}}^n + F_{\mathcal{WB}}^n\Big)\delta t + \epsilon^n,$$

which can be rewritten as

$$\frac{3}{2}\Big(V_{\rm grnd}^n - V_{\rm grnd}^{n-1}\Big) - \frac{1}{2}\Big(V_{\rm grnd}^{n-1} - V_{\rm grnd}^{n-2}\Big) - F_{\mathcal{WB}}^n\delta t = F_{\mathcal{I}}^n\delta t + \epsilon^n, \tag{32}$$

where the fluxes $F_{\mathcal{I}}^n$ and $F_{\mathcal{WB}}^n$ are still defined by (26). Moreover it results from (31) that

$$\begin{aligned}\frac{3}{2}\Big(V_{\rm over}^n - V_{\rm over}^{n-1}\Big) - \frac{1}{2}\Big(V_{\rm over}^{n-1} - V_{\rm over}^{n-2}\Big) + \Big(- \frac{3}{2}F_{\rm ABr}^n + \frac{1}{2}F_{\rm ABr}^{n-1}\Big)\delta t \\ = \Big(- \frac{3}{2}\Phi_{\mathcal{I}}^n + \frac{1}{2}\Phi_{\mathcal{I}}^{n-1}\Big)\delta t.\end{aligned} \tag{33}$$

The new interface flux $\Phi_{\mathcal{I}}^n$ is determined so that the mass flux $F_{\mathcal{I}}^n$ is exactly counter-balanced by the interface flux in (33), whence

$$F_{\mathcal{I}}^n = \frac{3}{2}\Phi_{\mathcal{I}}^n - \frac{1}{2}\Phi_{\mathcal{I}}^{n-1} \quad\Longrightarrow\quad \Phi_{\mathcal{I}}^n = \frac{2}{3}F_{\mathcal{I}}^n + \frac{1}{3}\Phi_{\mathcal{I}}^{n-1}.$$

At the first time step where a one-step implicit scheme is used, water volume conservation is directly enforced by setting $\Phi_{\mathcal{I}}^1 \stackrel{\rm def}{=} F_{\mathcal{I}}^1$.

Algorithm 3 Two-step coupling algorithm

Input: $\psi_{\mathfrak{h}}^{n-1}, \psi_{\mathfrak{h}}^{n-2}$ and $h_{\mathfrak{h}}^{n-1}$

$\vdots$

repeat

$\vdots$

$\omega_v^{n,p} \leftarrow -(3\tilde{h}_{\mathfrak{h}}^n/\delta t + v_{\mathfrak{h}}^{\star,n-1})/2$ on $\mathcal{I}_{\mathfrak{h}}^{\mathrm{d},n,p}$

$\psi_{\mathfrak{h}}^{n,p} \leftarrow$ `Richards_BDF2`$(\mathcal{I}_{\mathfrak{h}}^{\mathrm{d},n,p}, \mathcal{I}_{\mathfrak{h}}^{\mathrm{w},n,p}, \omega_v^{n,p}, \omega_\psi^{n,p}, \psi_{\mathfrak{h}}^{n-1}, \psi_{\mathfrak{h}}^{n-2})$

$\vdots$

$\forall i \in \{1 \cdots N_{\mathcal{I}}\},\ h_i^{n,p} = \tilde{h}_i^n + \delta t/l_i \int_{e_i} (2v_{\mathfrak{h}}^{\star,n,p} + v_{\mathfrak{h}}^{\star,n-1})/3$

$\vdots$

until $\forall\ i \in \{1 \cdots N_{\mathcal{I}}\}, h_i^{n,p} \geq 0$

$\vdots$

Output: $\psi_{\mathfrak{h}}^n, h_{\mathfrak{h}}^n$ and $v_{\mathfrak{h}}^{\star,n} = v_{\mathfrak{h}}^{\star,n,p}$

The resulting algorithm, referred to as two-step coupling algorithm, is outlined in Algorithm 3. Only the differences with Algorithm 2 are indicated. The key modification concerns the evaluation of the interface normal velocity in the calculation of $h_i^{n,p}$. The Neumann data $\omega_v^{n,p}$ is also modified to ensure that the Neumann condition indeed leads to a dry state in the corresponding cell. Also, the discrete approximation $\psi_{\mathfrak{h}}^{n-2}$ at time $(n-2)\delta t$ is added to the input and the interface normal velocity $v_{\mathfrak{h}}^{\star,n}$ is added to the output at each time step since it is used in the subsequent time step.

The main result concerning the overall water volume conservation for Algorithm 3 is the following.

Property 2 *Let δV^n be the overall water volume defect over the time step $[(n-1)\delta t, n\delta t]$ defined as*

$$\delta V^n \stackrel{\text{def}}{=} V^n - V^{n-1} - (\tilde{F}_{\mathcal{WB}}^n + F_{\mathrm{ABr}}^n)\delta t, \tag{34}$$

where $\tilde{F}_{\mathcal{WB}}^n \stackrel{\text{def}}{=} \frac{2}{3}F_{\mathcal{WB}}^n + \frac{1}{3}\tilde{F}_{\mathcal{WB}}^{n-1}$. Let $\triangle V^n$ be the overall water volume defect over the time interval $[0, n\delta t]$ defined as before. Then

$$|\triangle V^n| \leq \frac{1}{2}|\delta V^1| + nC\epsilon_{alg1},$$

where C is a constant and ϵ_{alg1} is the tolerance in Algorithm 1.

Proof: The coupling terms are eliminated when (32) and (33) are summed, leading to

$$\frac{3}{2}\Big(V^n - V^{n-1}\Big) - \frac{1}{2}\Big(V^{n-1} - V^{n-2}\Big) - \Big(F_{\mathcal{WB}}^n + \frac{3}{2}F_{\mathrm{ABr}}^n - \frac{1}{2}F_{\mathrm{ABr}}^{n-1}\Big)\delta t = \epsilon^n.$$

Using the definition of δV^n yields the recurrence relation $\delta V^n = \frac{1}{3}\delta V^{n-1} + \frac{2}{3}\,\epsilon^n$, so that

$$\delta V^n = \frac{1}{3^n}\delta V^1 + \frac{2}{3}\sum_{i=1}^{n} 3^{i-n} \times \epsilon^i.$$

Owing to the triangle inequality, it is inferred that

$$|\triangle V^n| \leq \frac{3}{2}\Big(\frac{1}{3} - \frac{1}{3^{n+1}}\Big)|\delta V^1| + \sum_{i=1}^{n}\Big(1 - \frac{1}{3^{i+1}}\Big)|\epsilon^i|,$$

whence

$$|\triangle V^n| \leq \frac{1}{2}|\delta V^1| + \sum_{i=1}^{n}|\epsilon^i| \leq \frac{1}{2}|\delta V^1| + nC\epsilon_{alg1}. \qquad \square$$

Finally, we observe that similar developments can be considered for arbitrary order BDFs with additional technicalities and longer recursion formulas.

4 Results

Algorithm 3 is assessed on three test cases: the first one concerns overland flow over a variable topography, the second one infiltration due to rainfall and the third one exfiltration resulting from injected water at the bottom of the aquifer. The soil consists of sand and is parameterized by the Haverkamp's constitutive relations [18]

$$\theta(\psi) = \frac{\theta_s - \theta_r}{1 + |\tilde{\alpha}\psi|^\beta} + \theta_r \quad \text{and} \quad K(\psi) = \frac{K_s}{1 + |\tilde{A}\psi|^\gamma},$$

with parameters

$$\begin{aligned} &\theta_s = 0.5, \quad \tilde{\alpha} = 0.028cm^{-1},\ K_s = 10^{-2}cm.s^{-1},\ \gamma = 4,\\ &\theta_r = 0.05,\ \beta = 4, \qquad\qquad \tilde{A} = 0.030cm^{-1}. \end{aligned}$$

Figure 5 presents the volumetric water content and the hydraulic conductivity as a function of the hydraulic head. The Strickler coefficient $\mathcal{K}$ is set to $60m^{1/3}s^{-1}$. For all test cases, the bottom boundary $\mathcal{B}$ is located at $z = 0$.

Piecewise affine finite elements are used ($p = 1$ in (15)) along with the usual local Lagrangian basis functions. For the first time step, the Crank–Nicolson scheme is used. A direct solver based on the LU decomposition is employed to solve the linear systems. The convergence tolerance ϵ_{alg1} in Algorithm 1 is set to 10^{-6} and the parameter η is set to 10. Moreover, we focus on the use of the second-order coupling algorithm. This choice is motivated by the

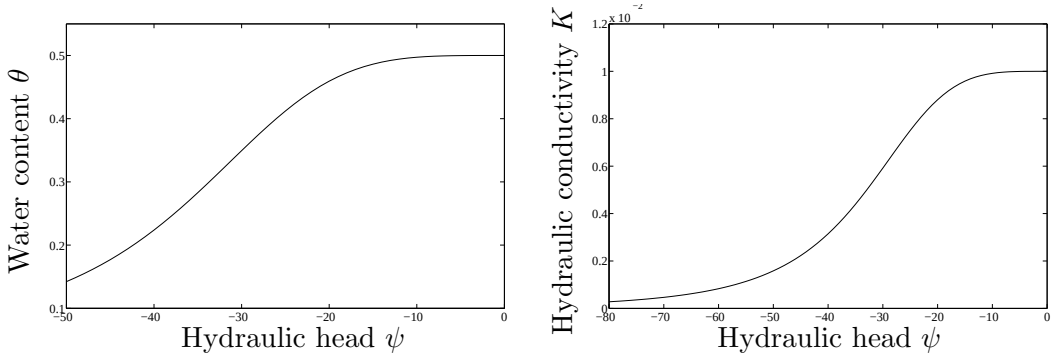

Figure 5. Hydraulic properties of the soil used in the test cases.

fact that it yields second-order discretization errors in time along with second-order discretization errors in space in the L^2-norm since $p = 1$. In addition, a second-order initialization of Algorithm 1 is chosen in the form

$$\forall n \geq 3, \quad \psi_{\mathfrak{h}}^{n,0} = 3\psi_{\mathfrak{h}}^{n-1} - 3\psi_{\mathfrak{h}}^{n-2} + \psi_{\mathfrak{h}}^{n-3}, \tag{35}$$

except for the second time step where the first-order initialization $\psi_{\mathfrak{h}}^{2,0} = 2\psi_{\mathfrak{h}}^{1} - \psi_{\mathfrak{h}}^{0}$ is used. The second-order initialization (35) can decrease significantly the CPU time (in comparison with the initialization $\psi_{\mathfrak{h}}^{n,0} = \psi_{\mathfrak{h}}^{n-1}$).

4.1 Test case 1 (TC1)

In this first test case, the runoff flow and the drainage of the subsurface domain are induced by the presence of the outlet, located below the initial height of the water table. The geometry is presented in Figure 6. The interface $\mathcal{I}$ is divided into three parts, $\mathcal{I}_1 = \{(x, z) \in \mathcal{I}, x \in [0, 1.4]\}$ (slope $J_1 = 0.1\%$), $\mathcal{I}_2 = \{(x, z) \in \mathcal{I}, x \in [1.4, 1.6]\}$ (slope $J_2 = 0.3\%$), and $\mathcal{I}_3 = \{(x, z) \in \mathcal{I}, x \in [1.6, 3]\}$ (slope $J_3 = 0.1\%$). The final simulation time is $T = 300s$. The initial condition is a horizontal water table located at $0.3025m$ with a hydrostatic pressure profile, and the boundary condition on walls and bottom is a zero flux,

$$\begin{aligned} \psi^0 = -z + 0.3025m \quad & \text{in } \Omega, \\ v_N = 0 \quad & \text{on } (\mathcal{W} \cup \mathcal{B}) \times [0, T]. \end{aligned}$$

For the overland flow, the initial condition is a horizontal free surface and the boundary condition is a zero water depth

$$\begin{aligned} h^0 \ = (-z + 0.3025m)^+ \quad & \text{on } I, \\ h_{\mathrm{A}} \ = 0 \quad & \text{at A} \times [0, \mathrm{T}]. \end{aligned}$$

A mesh with 2063 triangles (corresponding to a typical mesh-size of $3.5cm$)

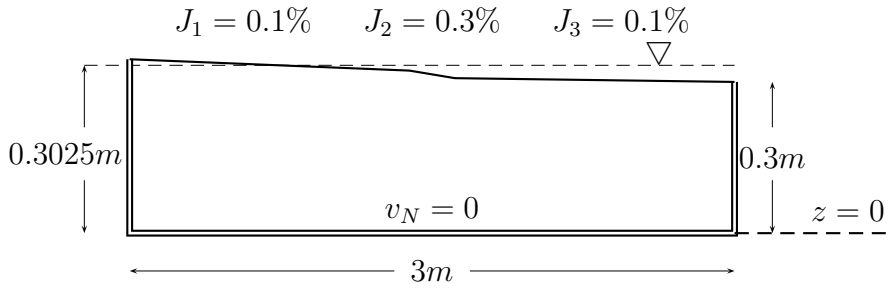

Figure 6. TC1 - Geometry and initial water table position.

along with time steps $\delta t = 2.5s$ and $\delta t' = 0.25s$ have been used. We have verified that the interface normal velocity obtained with $\delta t = \delta t' = 0.25s$ can be superimposed to that reported below. In this case, the use of $\delta t = 2.5s$ instead of $\delta t = \delta t' = 0.25s$ leads to a gain of 89% in the computational time.

Figure 7 presents the free surface of the overland flow ($h_{\mathfrak{h}}^n$ + topography) and the interface normal velocity $v_{\mathfrak{h}}^{\star,n}$ along the interface at three characteristic times of the simulation ($10s, 100s$, and $300s$). The free surface being piecewise constant, it is depicted on each interface cell by a solid line. The interface normal velocity $v_{\mathfrak{h}}^{\star,n}$ is plotted with circles if the interface is wet (that is, on $\mathcal{I}_{\mathfrak{h}}^{\mathrm{w},n}$) and with crosses if the interface is dry (that is, on $\mathcal{I}_{\mathfrak{h}}^{\mathrm{d},n}$).

Figure 8 provides a closer insight at the issue of staying on the admissible set $\mathcal{A}$. For the same times as in Figure 7 and for each face of $\mathcal{F}_{\mathfrak{h}}^{\mathcal{I}}$, each couple $(\psi_{\mathfrak{h}}^n, h_{\mathfrak{h}}^n)$ is represented by a cross (the mean-value of $\psi_{\mathfrak{h}}^n$ is considered on each face). The admissible set $\mathcal{A}$ is also plotted with a solid line.

The hydraulic jump in the overland flow is visible at the beginning of the simulation on Figure 7 at 10s. Moreover, exfiltration appears on some faces located on $\mathcal{I}_2$ and $\mathcal{I}_3$. During the simulation, a Neumann boundary condition is imposed on the faces where the water becomes zero. It is confirmed by Figure 8 where the number of couples $(\psi_{\mathfrak{h}}^n, h_{\mathfrak{h}}^n)$ situated on the branch $\{h = 0\}$ increases.

4.2 Test case 2 (TC2)

The principle of this test case is inspired by the work of Abdul and Gilham [1]: a constant rainfall intensity is imposed on the upper part of the domain for a fixed period of time, whereas the lateral and lower boundaries are impermeable. The geometry is shown in Figure 9 and the final simulation time is $T = 360s$. The initial condition is a horizontal water table located at $0.85m$ with a hydrostatic pressure profile, and the boundary condition on walls and

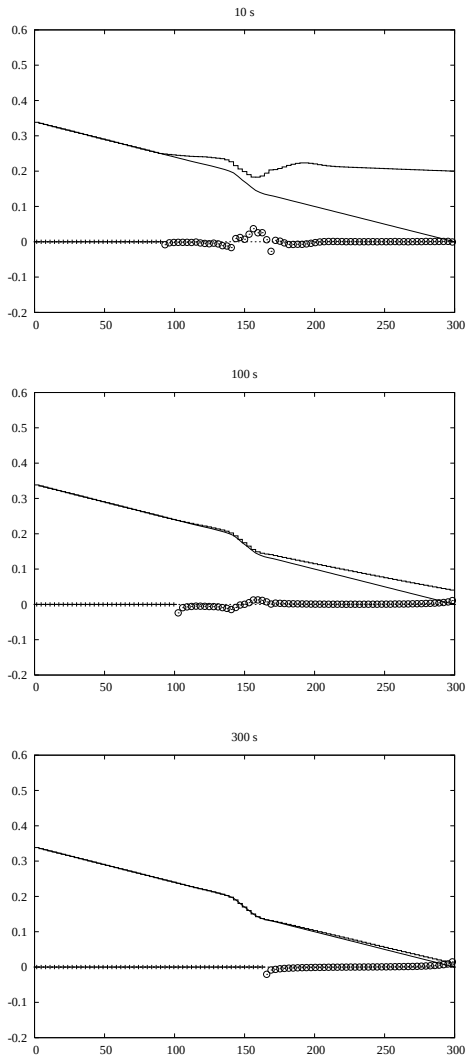

Figure 7. TC1 - Free surface (solid line) and interface normal velocity ($cm/12min$) plotted with circles if interface is wet and with crosses if interface is dry.

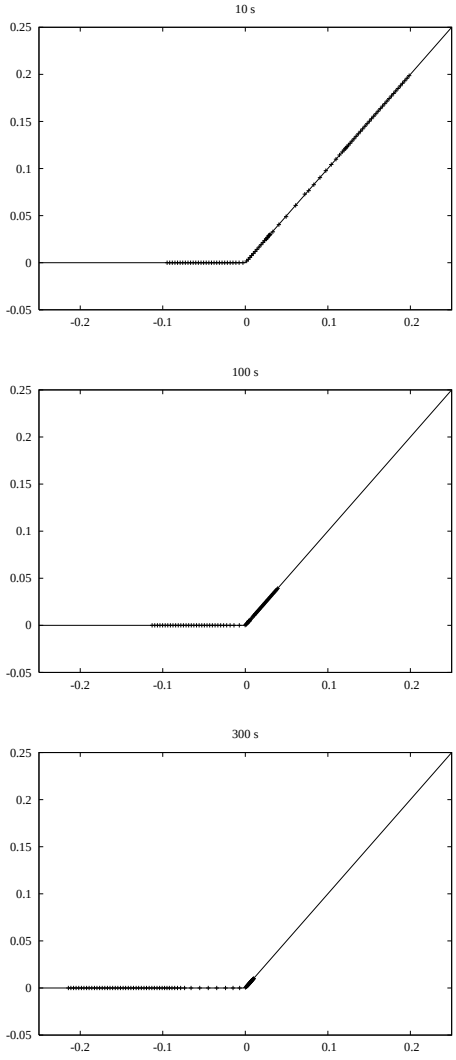

Figure 8. TC1 - Cloud of points $(\psi_{\mathfrak{h}}^n, h_{\mathfrak{h}}^n)$ on the admissible set $\mathcal{A}$ at different times.

bottom is a zero flux,

$$\begin{aligned} \psi^0 = -z + 0.85m \quad & \text{in } \Omega, \\ v_N = 0 \quad & \text{on } (\mathcal{W} \cup \mathcal{B}) \times [0, T]. \end{aligned}$$

For the overland flow, the initial condition and the boundary condition are

$$\begin{aligned} h^0 \ &= 0 \quad \text{on } \mathcal{I}, \\ h_{\mathrm{A}} \ &= 0 \quad \text{at A} \times [0, \mathrm{T}]. \end{aligned}$$

A constant rainfall intensity equal to 10% of the hydraulic conductivity at saturation is imposed during $180s$ and is stopped afterwards,

$$\begin{aligned} v_{\mathrm{r}} \cdot n_\Omega &= -0.1K_s \quad \text{on } \mathcal{I} \times [0, 180], \\ v_{\mathrm{r}} \cdot n_\Omega &= 0 \quad \text{on } \mathcal{I} \times [180, T]. \end{aligned}$$

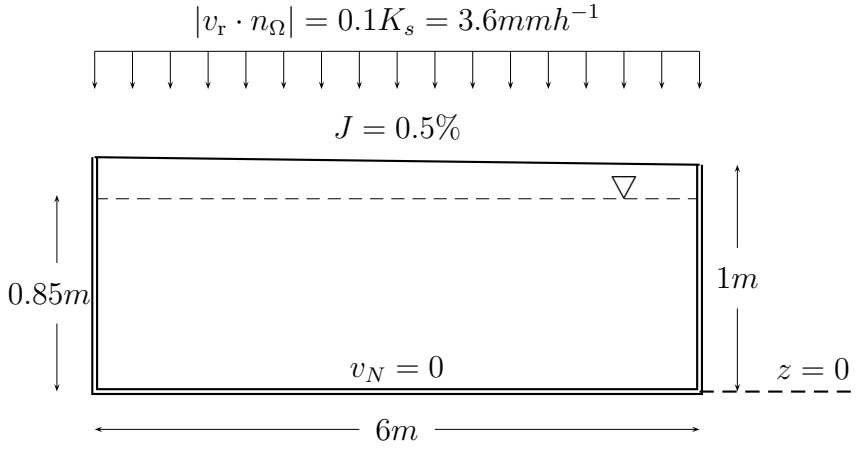

Figure 9. TC2 - Geometry, initial water table position, and rainfall intensity.

A mesh with 2049 triangles (corresponding to a typical mesh-size of $10cm$) and time steps $\delta t = \delta t' = 1s$ have been used. We have verified that the interface normal velocity obtained with a finer mesh (8763 elements) and a smaller time step ($\delta t = \delta t' = 0.5s$) can be superimposed to that reported below. Also, observe that $\delta t' = 1s$ roughly corresponds to the CFL condition, so that, for the present test case, the accuracy limit on the time step for Richards' equation is comparable to the CFL restriction.

Figure 10 presents, along the interface at four characteristic times of the simulation ($10s, 60s, 180s$, and $360s$), the free surface and the piecewise constant normal velocity $v_{\mathfrak{h}}^{\star\star,n}$ defined on the face with center x_i as

$$v_{\mathfrak{h}}^{\star\star,n} \stackrel{\text{def}}{=} \frac{1}{l_i} \int_{x_{i-\frac{1}{2}}}^{x_{i+\frac{1}{2}}} \left(\frac{2}{3} v_{\mathfrak{h}}^{\star,n} + \frac{1}{3} v_{\mathfrak{h}}^{\star,n-1} \right).$$

The same notation is used as in Figure 7. The hydrological response of the system can be divided into four phases.
1 - Soil saturation $[0, 50s]$. In this phase, which results from the initial water table position, the $15cm$ top layer is being saturated. The rainfall is totally absorbed by the soil, the surface water depth is equal to zero, and a Neumann condition is imposed on all the faces of $\mathcal{I}$ (Figure 10 at $10s$).
2 - Surface runoff occurs on part of $\mathcal{I}$ $[50s, 90s]$. The rainfall is still partially absorbed by the soil, but a Dirichlet condition is now being imposed on the part of $\mathcal{I}$ located near the outlet. Interestingly, infiltration occurs on the most part of the interface since the normal velocity is negative, but some exfiltration

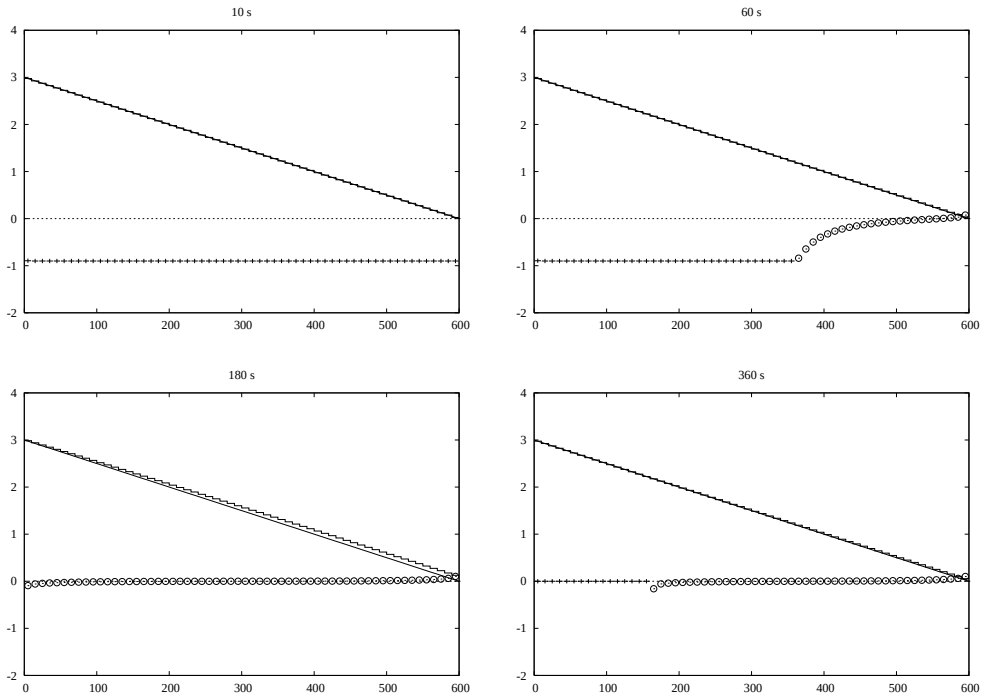

Figure 10. TC2 - Free surface (solid line) and interface normal velocity ($cm/15min$) plotted with circles if interface is wet and with crosses if interface is dry.

occurs on the first few faces located near the outlet where the normal velocity becomes positive (Figure 10 at $60s$).
3 - Surface runoff occurs on $\mathcal{I}$ $[90s, 180s]$. Surface runoff occurs on the whole interface and the soil is totally saturated. A Dirichlet condition is imposed throughout the interface and the surface water depth is positive (Figure 10 at $180s$).
4 - Drainage $[180s, 360s]$. When rainfall stops, the surface water depth returns to zero on the faces located near the point A because of infiltration and surface runoff. A Neumann boundary condition is imposed on the dry zone near the point A (Figure 10 at $360s$).

Figure 11 provides a closer insight at the issue of staying on the admissible set $\mathcal{A}$. For the same times as in Figure 10 and for each face of $\mathcal{F}_{\mathfrak{h}}^{\mathcal{I}}$, each couple $(\psi_{\mathfrak{h}}^n, h_{\mathfrak{h}}^n)$ is represented as in Figure 8. Note that different scales are used, so that the branch $\{h = \psi\}$ is almost vertical. The four phases described above are clearly illustrated by the position of the cloud of points. At $10s$, the hydraulic head is negative and the water depth is equal to zero. The cloud of points is only on the branch $\{h = 0\}$ corresponding to a dry soil. At $60s$, the hydraulic head is equal to the water depth for some faces. The cloud of points is located on the two branches because the soil contains both saturated and unsaturated zones. At $180s$, the hydraulic head is equal to the water depth for all the faces. The cloud of points is only on the branch $\{h = \psi\}$ corresponding to a wet soil. At $360s$, the hydraulic head becomes negative where the surface

water depth is equal to zero. The cloud of points is again located on the two branches.

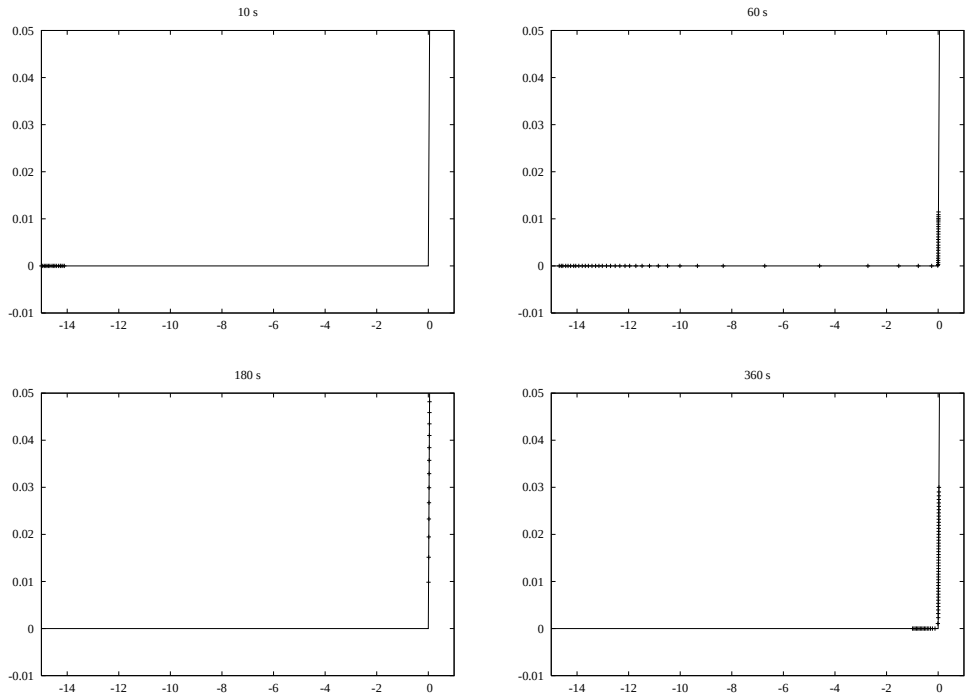

Figure 11. TC2 - Cloud of points $(\psi_{\mathfrak{h}}^n, h_{\mathfrak{h}}^n)$ on the admissible set $\mathcal{A}$ at different times.

The left panel of Figure 12 presents the number of iterations as a function of time in Algorithm 3. The four phases of the simulation are again visible. When the interface is dry ($[0, 50s]$), two iterations are needed since all the faces are initialized as wet and are actually dry. When surface runoff occurs ($[50s, 90s]$), there are wet and dry parts along the interface, and the number of iterations fluctuates between 6 and 8. When the whole interface is wet ($[90s, 210s]$), only one iteration is necessary. Finally, during drainage ($[210s, 360s]$), there are again wet and dry parts along the interface, and the number of iterations fluctuates between 2 and 3. The number of iterations is almost identical when resorting to Algorithm 2 or to finer meshes and time steps, except for some shifts by a few seconds resulting from better resolution of the time evolution of the system. Finally, the number of quasi-Newton iterations (Algorithm 1) averaged per time step is, except for times close to initialization, less than 3, both with the single-step and the two-step coupling algorithms. The right panel of Figure 12 presents the time evolution of this quantity when employing the two-step coupling algorithm.

Figure 13 presents results on mass conservation issues. Multiplying equation (34) by the water density ρ, summing over the time intervals in $[0, n\delta t]$, know-

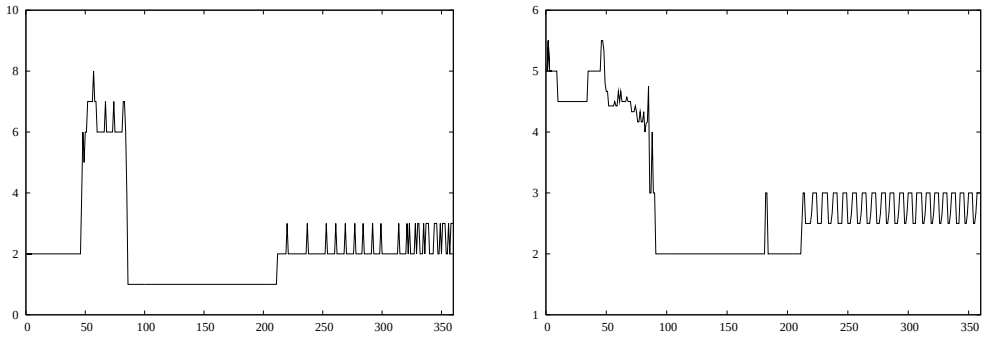

Figure 12. TC2 - Left: Number of iterations as a function of time in Algorithm 3; Right: Mean number of quasi-Newton iterations per time step as a function of time.

ing that $\tilde{F}^n_{\mathcal{WB}} = 0$ and the definition of V^n, F^n_{ABr}, and ΔV^n yields

$$\underbrace{\rho(V^n_{\mathrm{grnd}} - V^0_{\mathrm{grnd}})}_{\Delta\mathbb{M}^n_{\mathrm{grnd}}} + \underbrace{\rho(V^n_{\mathrm{over}} - V^0_{\mathrm{over}})}_{\Delta\mathbb{M}^n_{\mathrm{over}}} = \sum_{i=1}^{n} \underbrace{\rho\delta t\Big(F^i_{\mathrm{A}} + F^i_{\mathrm{r}}\Big)}_{\mathbb{M}^i_{\mathrm{in}}} + \sum_{i=1}^{n} \underbrace{\rho\delta t F^i_{\mathrm{B}}}_{\mathbb{M}^i_{\mathrm{out}}} + \underbrace{\rho\Delta V^n}_{\mathbb{E}^n}.$$

$\Delta\mathbb{M}^n$ is defined as the total mass variation over the time interval $[0, n\delta t]$ and is the sum of the total groundwater mass variation $\Delta\mathbb{M}^n_{\mathrm{grnd}}$ and the total overland mass variation $\Delta\mathbb{M}^n_{\mathrm{over}}$. The quantities $\sum_{i=1}^n \mathbb{M}^i_{\mathrm{in}}$, $\sum_{i=1}^n \mathbb{M}^i_{\mathrm{out}}$, and $\mathbb{E}^n$ are respectively the total inflow of water, the total outflow of water, and the total mass balance defect cumulated at time $n\delta t$. The five quantities $\Delta\mathbb{M}^n, \Delta\mathbb{M}^n_{\mathrm{grnd}}, \Delta\mathbb{M}^n_{\mathrm{over}}, \sum_{i=1}^n \mathbb{M}^i_{\mathrm{in}}$, and $\sum_{i=1}^n \mathbb{M}^n_{\mathrm{out}}$ are presented in the left part of Figure 13. In particular, this figure confirms the four phases of the simulation. The rainfall is totally absorbed by the soil at the beginning of the simulation until $50s$ since $\Delta\mathbb{M}^n = \Delta\mathbb{M}^n_{\mathrm{grnd}}$. Then, the increase of $\Delta\mathbb{M}^n_{\mathrm{grnd}}$ diminishes and $\Delta\mathbb{M}^n_{\mathrm{over}}$ becomes positive as a result of soil saturation. From 90s to the end of the simulation, the variations of $\Delta\mathbb{M}^n$ and $\Delta\mathbb{M}^n_{\mathrm{over}}$ are the same, corresponding to a complete saturation of the soil. Moreover, during the last phase, the total water inflow is constant because the rainfall stops, so that the total water outflow is the same as the total mass variation.

To study the influence of the new flux at the interface in the two-step algorithm, we define Algorithm 2' as Algorithm 2 employed with procedure `Richards_BDF2` instead of procedure `Richards_BDF1`, that is, the modifications of Algorithm 3 needed to ensure mass conservation are not taken into account. Total mass balance defects obtained with Algorithms 3 and 2' are compared in the right part of Figure 13. Algorithm 3 yields a sizable improvement over Algorithm 2'; yet, it can be noticed that the mass balance defect produced by Algorithm 2' is only of the order of a few percent of global quantities such as $\Delta\mathbb{M}^n$.

Finally, Figure 14 studies in more detail the mass fluxes in the kinematic wave equation. The mass flux $\tilde{F}^n_{\mathcal{I}}$ is decomposed into the exfiltration flux

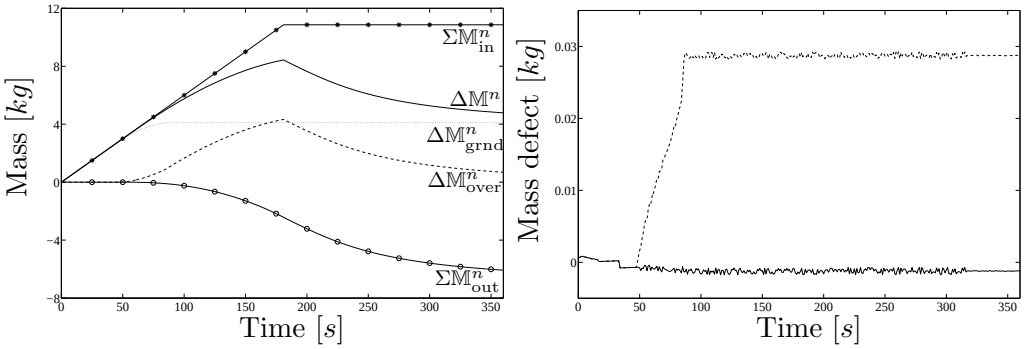

Figure 13. TC2 - Left: Mass repartition in the coupled system; Right: Mass balance defect $\mathbb{E}^n$ for Algorithm 2' (dashed) and Algorithm 3 (solid).

$\tilde{F}^{n,+}_{\mathcal{I}}$ and the infiltration flux $\tilde{F}^{n,-}_{\mathcal{I}}$ in the form $\tilde{F}^n_{\mathcal{I}} \overset{\text{def}}{=} \tilde{F}^{n,+}_{\mathcal{I}} + \tilde{F}^{n,+}_{\mathcal{I}}$, with $\tilde{F}^{n,+}_{\mathcal{I}} \overset{\text{def}}{=} -\int_{\mathcal{I}^{n,+}_{\mathfrak{h}}} v^{\star,n}_{\mathfrak{h}}$ and $\tilde{F}^{n,-}_{\mathcal{I}} \overset{\text{def}}{=} -\int_{\mathcal{I}^{n,-}_{\mathfrak{h}}} v^{\star,n}_{\mathfrak{h}}$, where the time-dependent sets $\mathcal{I}^{n,+}_{\mathfrak{h}}$ and $\mathcal{I}^{n,-}_{\mathfrak{h}}$ are defined as follows

$$\mathcal{I}^{n,+}_{\mathfrak{h}} \overset{\text{def}}{=} \{x \in \mathcal{I};\ v^{\star,n}_{\mathfrak{h}}(x) < 0\} \quad \text{and} \quad \mathcal{I}^{n,-}_{\mathfrak{h}} \overset{\text{def}}{=} \{x \in \mathcal{I};\ v^{\star,n}_{\mathfrak{h}}(x) > 0\}.$$

The four quantities $\rho\delta t\tilde{F}^{n,+}_{\mathcal{I}}, \rho\delta t\tilde{F}^{n,-}_{\mathcal{I}}, \mathbb{M}^n_{\text{in}}$, and $\mathbb{M}^n_{\text{out}}$ are plotted on Figure 14 as a function of time.

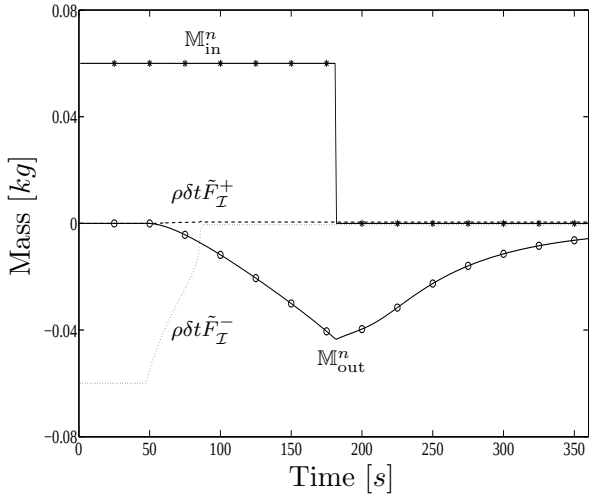

Figure 14. TC2 - Mass fluxes in the kinematic wave equation.

4.3 Test case 3 (TC3)

In this third test case, an exfiltration is produced on the upper part of the domain by injecting water at the bottom-left part. The geometry is presented in Figure 15. The final simulation time is $T = 360s$. The initial condition is a horizontal water table located at $0.1m$ with an hydrostatic pressure profile,

and the boundary condition on the walls corresponds to a zero flux,

$$\begin{aligned} \psi^0 &= -z + 0.1m \quad \text{in } \Omega, \\ v_N &= 0 \quad \text{on } \mathcal{W} \times [0, T]. \end{aligned}$$

The rainfall intensity is set to zero. An infiltration flux with a parabolic profile and a mean-value $\bar{v}_N$ equal to 5% of hydraulic conductivity at saturation is imposed during 2 minutes on the left half $\mathcal{B}_l$ of the bottom ($\mathcal{B}_l = \{(x, z) \in \mathcal{B}, x \in [0, 1]\}$ and $\mathcal{B}_r = \{(x, z) \in \mathcal{B}, x \in [1, 2]\}$). This infiltration flux is linear during the first $10s$, constant for $t \in [10, 120]s$, and equal to zero for $t > 120s$:

$$v_N(x,t) = \begin{cases} x(x-1)\ 0.03K_s t, & \text{if } (x,t) \in \mathcal{B}_l \times [0, 10], \\ x(x-1)\ 0.3K_s, & \text{if } (x,t) \in \mathcal{B}_l \times [10, 120], \\ 0, & \text{otherwise.} \end{cases}$$

For the overland flow, the initial condition and the boundary condition are

$$\begin{aligned} h^0 &= 0 \quad \text{on } \mathcal{I}, \\ h_{\mathrm{A}} &= 0 \quad \text{at A} \times [0, \mathrm{T}]. \end{aligned}$$

A mesh with 1874 triangles (corresponding to a typical mesh-size of $2.5cm$) and time steps $\delta t = \delta t' = 1s$ have been used. We have verified that the interface normal velocity obtained with a finer mesh (7310 elements) and a smaller time step ($\delta t = \delta t' = 0.5s$) can be superimposed to that reported below.

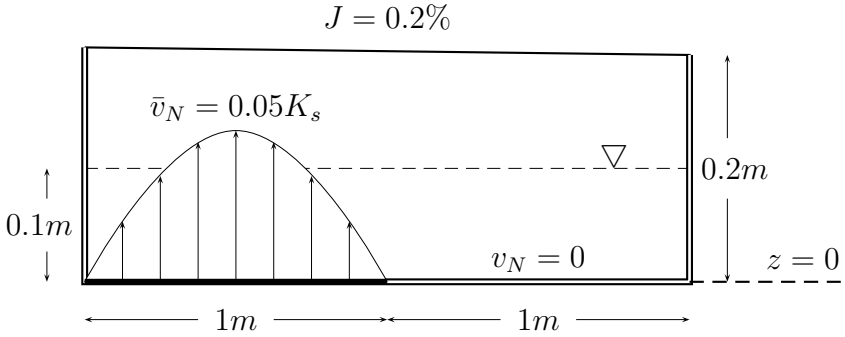

Figure 15. TC3 - Geometry, initial water table position, and flux infiltration.

Figure 16 presents the free surface and the normal velocity $v_{\mathfrak{h}}^{\star,n}$ along the interface at six characteristic times of the simulation ($5s, 35s, 50s, 100s, 150s$, and $360s$) and Figure 17 presents the surface water depth $h_{\mathfrak{h}}^n$ at these different times. The same notation is used as in Figure 7. The hydrological response of the system can be divided into six phases.

1 - Soil saturation $[0, 15s]$. This phase results from the initial water table position. At the beginning of the simulation, the soil is partially saturated, and

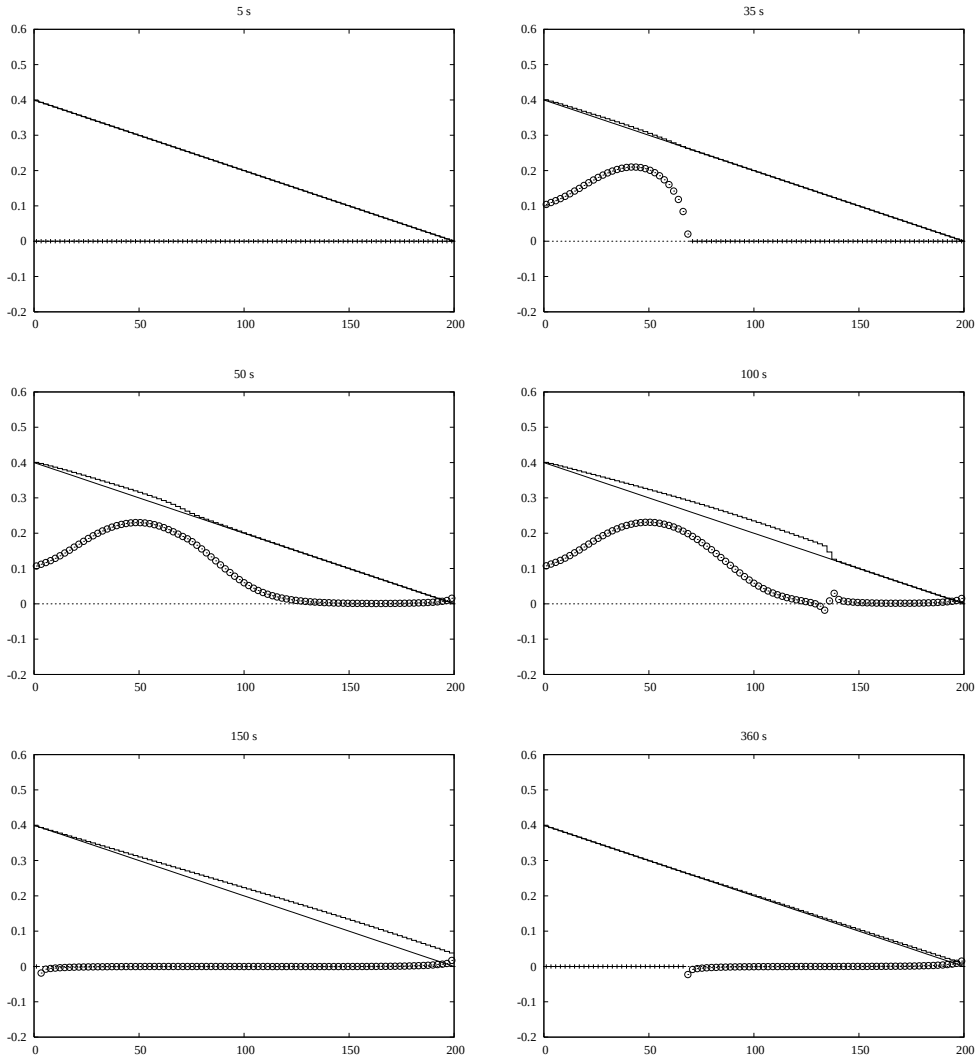

Figure 16. TC3 - Free surface (solid line) and interface normal velocity ($cm/6min$) plotted with circles if interface is wet and with crosses if interface is dry.

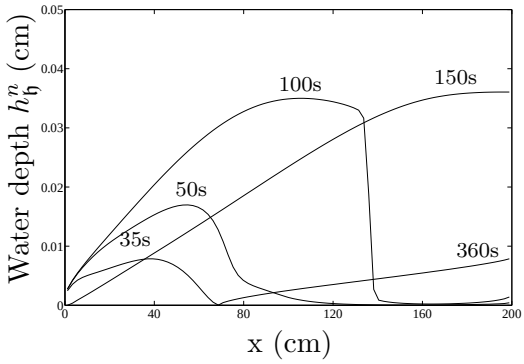

Figure 17. TC3 - Surface water depth $h_{\mathfrak{h}}^n$ at different times.

the injection at the bottom of the domain increases the hydraulic head. The interface is totally dry and a zero Neumann boundary condition is enforced everywhere on $\mathcal{I}$ (Figure 16 at $5s$).
2 - Partial exfiltration $[15s, 45s]$. The soil becomes saturated in the left part of the domain and the interface normal velocity positive, so that water begins to exfiltrate from the faces situated in this saturated zone. A Dirichlet condition is enforced on those faces (Figure 16 at $35s$).
3 - Full exfiltration $[45, 100s]$. When the soil is totally saturated, the amount of exfiltrated water is equal to the amount of injected water. We observe that overland flow occurs over the whole interface $\mathcal{I}$ and that a Dirichlet condition is being enforced everywhere. However, most of the overland flow still remains concentrated near the upper part of the interface (Figure 16 at $50s$).
4 - Propagation of the runon wave $[100, 120s]$. In this phase, the runon wave propagates downstream. It is worthwhile to notice that a slight part of the surface water infiltrates back into the soil as indicated by the sign of the normal velocity near the heading part of the runon wave (Figure 16 at $100s$).
5 - Outflow $[120, 200s]$. When water injection ceases at the bottom of the domain, the amount of exfiltrated water decreases sharply and there is even a small portion of the interface located near the point A where water infiltrates back into the soil (despite the boundary condition is of Dirichlet type since the surface water depth is still positive) while most of the overland flow reaches the outlet and exits the system (Figure 16 at $150s$).
6 - Drainage $[200, 360s]$. The surface water depth vanishes on the upper part of the interface $\mathcal{I}$ where a zero Neumann condition is now imposed (Figure 16 at $360s$).

Figure 18 shows that each couple $(\psi_{\mathfrak{h}}^n, h_{\mathfrak{h}}^n)$ stays on the admissible set $\mathcal{A}$. As in the previous test case, the phases described above are clearly illustrated by the position of the cloud of points. It is located on the branch $\{h = 0\}$ when the soil is unsaturated, on the branch $\{h = \psi\}$ when the soil is saturated, and on the two branches when there are both saturated and unsaturated zones at the interface.

Results on Figure 19 and Figure 20 are similar to the ones of the previous test case, in particular the comparison of the mass balance defects for Algorithms 3 and 2'.

5 Conclusion

In this work we have presented a robust and accurate numerical method to simulate coupled subsurface and overland flows governed by Richards' equation and the kinematic wave equation. Special care was taken to design coupling algorithms that preserve the overall mass in the system and that also satisfy

the various equality and inequality constraints imposed at the interface. Since these algorithms hinge on a splitting between the kinematic wave part without exchange terms on the one hand and Richards' equation with exchange terms on the other hand, they converge globally to first-order in time, as confirmed by numerical observations. Extensions of the present work include the use of more complex models, such as the shallow-water equations, to describe the overland flow and the possibility to account for drainage pipes in the soil. Extension to two-dimensional surface flows and three-dimensional subsurface variably saturated flows can also be considered. The present algorithms are currently being tested in more complex and realistic test cases related to field studies.

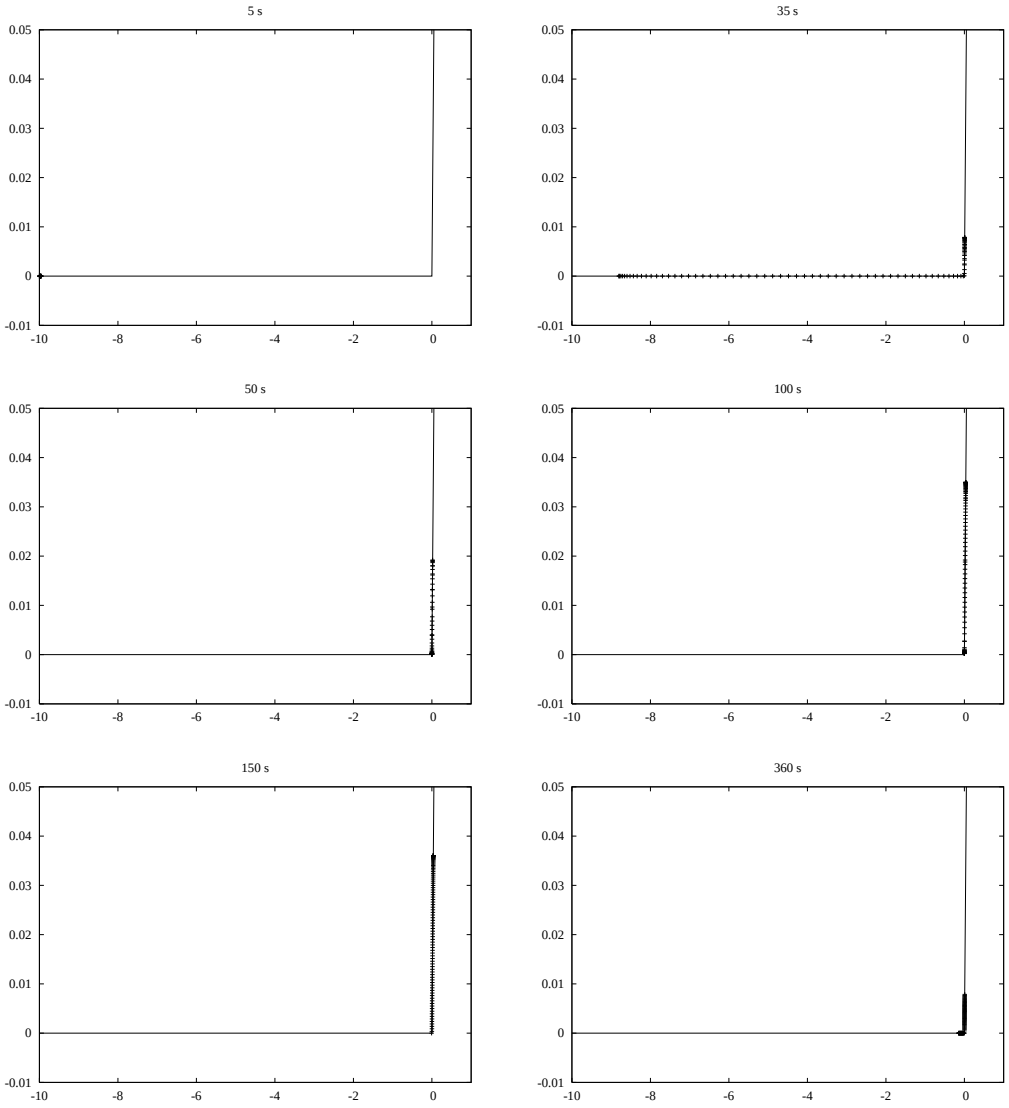

Figure 18. TC3 - Cloud of points $(\psi_{\mathfrak{h}}^n, h_{\mathfrak{h}}^n)$ on the admissible set $\mathcal{A}$ at different times.

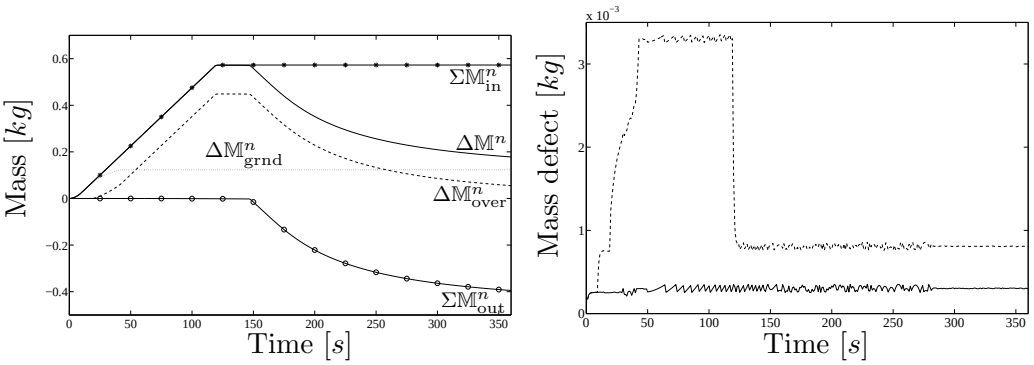

Figure 19. TC3 - Left: Mass repartition in the coupled system; Right: Mass balance defect $\mathbb{E}^n$ for Algorithm 2' (dashed) and Algorithm 3 (solid).

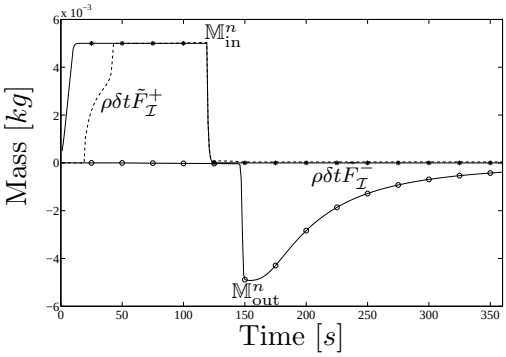

Figure 20. TC3 - Mass fluxes in the kinematic wave equation.

References

[1] A. S. Abdul, R. W. Gillham, Laboratory studies of the effects of the capillary fringe on streamflow generation, Water Ressources Research 20 (6) (1984) 691–698.

[2] P. Bastian, Higher order discontinuous Galerkin methods for flow and transport in porous media, in: Challenges in scientific computing—CISC 2002, vol. 35 of Lect. Notes Comput. Sci. Eng., Springer, Berlin, 2003, pp. 1–22.

[3] P. Bastian, R. Helmig, Efficient fully-coupled solution techniques for two-phase flow in porous media, Advances in Water Ressources 23 (1) (1999) 199–216.

[4] P. Bastian, I. O., F. Rezanezhad, H. J. Vogel, K. Roth, Numerical simulation and experimental studies of unsaturated water flow in heterogeneous systems, in: Reactive flows, diffusion and transport, Springer, Berlin, 2007, pp. 579–597.

[5] P. Bastian, B. Rivière, Discontinuous galerkin methods for two-phase flow in porous media, Tech. Rep. 2004–28, IWR (SFB 359), Universität Heidelberg (2004).

[6] M. Bause, P. Knabner, Computation of variably saturated subsurface flow by adaptive mixed hybrid finite element methods, Advances in Water Ressources 27 (2004) 565–581.

[7] H. Beaugendre, A. Ern, T. Esclaffer, E. Gaume, I. Ginzburg, C. Kao, A seepage face model for the interaction of shallow water tables with the ground water surface: Application of the obstacle-type method, Journal of Hydrology 329 (2006) 258–273.

[8] G. Beavers, D. Joseph, Boundary conditions at a naturally impermable wall, J. Fluid. Mech. 30 (1967) 197–207.

[9] M. A. Celia, E. T. Bouloutas, A general mass-conservative numerical solution for the unsaturated flow equation, Water Ressources Research 26 (7) (1990) 1483–1496.

[10] B. Cockburn, C.-W. Shu, The local discontinuous Galerkin method for time-dependent convection-diffusion systems, SIAM Journal on Numerical Analysis 35 (6) (1998) 2440–2463 (electronic).

[11] C. Dawson, Analysis of discontinuous finite element methods for ground water/surface water coupling, SIAM Journal on Numerical Analysis 44 (4) (2006) 1375–1404.

[12] D. A. Di Pietro, A. Ern, J.-L. Guermond, Discontinuous Galerkin methods for anisotropic semidefinite diffusion with advection, SIAM J. Numer. Anal. 46 (2) (2008) 805–831.

[13] M. Discacciati, E. Miglio, A. Quarteroni, Mathematical and numerical models for coupling surface and groundwater flows, Applied Numerical Mathematics 43 (2002) 57–74.

[14] A. Ern, S. Nicaise, M. Vohralík, An accurate $\mathbf{H}(\mathrm{div})$ flux reconstruction for discontinuous Galerkin approximations of elliptic problems, C. R. Math. Acad. Sci. Paris 345 (12) (2007) 709–712.

[15] A. Ern, A. F. Stephansen, P. Zunino, A discontinuous Galerkin method with weighted averages for advection-diffusion equations with locally small and anisotropic diffusivity, IMA J. Numer. Anal.To appear.

[16] S. Fagherazzi, D. J. Furbish, P. Rasetarinera, M. Youssuff Hussaini, Application of the discontinuous spectral Galerkin method to groundwater flow, Advances in Water Ressources 27 (2004) 129–140.

[17] J.-F. Gerbeau, B. Perthame, Derivation of viscous Saint-Venant system for laminar shallow water; numerical validation, Discrete and Continuous Dynamical Systems: Series B 1 (1) (2001) 89–102.

[18] R. Haverkamp, M. Vauclin, J. Touma, P. J. Wierenga, G. Vachaud, A comparison of numerical simulation models for one-dimensionnal infiltration, Soil Science Society of America Journal 41 (1977) 285–294.

[19] W. Jäger, A. Mikelic, On the interface boundary condition of Beavers, Joseph and Saffmann, SIAM J. Appl. Math. 60 (2000) 1111–1127.

[20] K. R. Kavanagh, C. T. Kelley, R. C. Berger, J. P. Hallberg, S. E. Howington, Nonsmooth nonlinearities and temporal integration of richards equation, in: Proceedings of the XIV International Conference on Computational Methods in Water Resources, S. Majid Hassanizadeh, Ruud J. Schotting, W. G. Gray, and G. F. Pinder, editors, pp 947-954., 2002.

[21] W. Klieber, B. Rivière, Adaptive simulations of two-phase flow by discontinuous Galerkin methods, Comput. Methods Appl. Mech. Engrg. 196 (1-3) (2006) 404–419.

[22] P. Knabner, E. Schneid, Adaptive hybrid mixed finite element discretization of instationary variably saturated flow in porous media, High Performance Scientific and Engineering Computing 29 (2002) 37–44.

[23] S. J. Kollet, R. M. Maxwell, Integrated surface-groundwater flow modeling: A free-surface overland flow boundary condition in a groundwater flow model, Advances in Water Ressources 29 (2006) 945–958.

[24] G. Manzini, S. Ferraris, Mass-conservative finite volume methods on 2-d unstructured grids for the Richards equation, Advances in Water Ressources 27 (2004) 1199–1215.

[25] E. Miglio, A. Quarteroni, F. Saleri, Coupling of free surface and groundwater flows, Computers and Fluids 32 (2003) 73–83.

[26] V. M. Ponce, D. B. Simons, Shallow wave propagation in open channel flow, ASCE J. Hydraul. Div 103 (HY12) (1977) 1461–1476.

[27] A. Quarteroni, R. Sacco, F. Saleri, Numerical Mathematics, Springer, 2000.

[28] L. A. Richards, Capillary conduction of liquids through porous medium, Physics 1 (1931) 318–333.

[29] P. G. Saffman, On the boundary condition at the interface of a porous medium, Stud. Appl. Math. 1 (1971) 93–101.

[30] V. Singh, S. M. Bhallamudi, Conjonctive surface-subsurface modeling of overland flow, Advances in Water Ressources 21 (1998) 567–579.

[31] J. E. VanderKwaak, K. Loague, Hydrologic-response simulations for the R-5 catchment with a comprehensive physics-based model, Water Ressources Research 37 (4) (2001) 999–1013.

[32] C. S. Woodward, C. Dawson, Analysis of expanded mixed finite element methods for a nonlinear parabolic equation modeling flow into variably saturated porous media, SIAM J. Numer. Anal. 37 (3) (2000) 701–724 (electronic).